nature geoscience

ARTICLES

https://doi.org/10.1038/s41561-021-00733-0

Rates of protoplanetary accretion and differentiation set nitrogen budget of rocky planets

Damanveer S. Grewal[1]✉, Rajdeep Dasgupta[1], Taylor Hough[1] and Alexandra Farnell[1,2]

The effect of protoplanetary differentiation on the fate of life-essential volatiles such as nitrogen and carbon and its subsequent effect on the dynamics of planetary growth is unknown. Because the dissolution of nitrogen in magma oceans depends on its partial pressure and oxygen fugacity, it is an ideal proxy to track volatile redistribution in protoplanets as a function of their sizes and growth zones. Using high-pressure/temperature experiments in graphite-undersaturated conditions, here we show that the siderophilic (iron-loving) character of nitrogen is an order of magnitude higher than previous estimates across a wide range of oxygen fugacity. The experimental data combined with metal–silicate–atmosphere fractionation models suggest that asteroid-sized protoplanets, and planetary embryos that grew from them, were nitrogen depleted. However, protoplanets that grew to planetary embryo size before undergoing differentiation had nitrogen-rich cores and nitrogen-poor silicate reservoirs. Bulk silicate reservoirs of large Earth-like planets obtained nitrogen from the cores of the latter type of planetary embryos. Therefore, to satisfy the volatile budgets of Earth-like planets during the main stage of their growth, the timescales of planetary embryo accretion had to be shorter than their differentiation timescales; that is, Moon- to Mars-sized planetary embryos grew rapidly within ~1–2 Myrs of the Solar System's formation.

Bulk silicate reservoirs (mantle + crust + atmosphere) of rocky protoplanets and planets in the inner Solar System are extremely depleted in major volatiles such as nitrogen (N) and carbon (C)[1–5]. It is assumed that these bodies grew by accreting nearly volatile-free material due to a lack of condensation of volatiles in their growth zone[2,6]. Therefore, the volatile inventory of rocky planets is thought to be chiefly established by the addition of carbonaceous chondrite-like material from the outer Solar System to almost volatile-free bodies[1,2]. However, enstatite chondrites that source the inner Solar System reservoir[7] contain several hundred ppm of N and C in refractory phases[8]. The presence of isotopically distinct N in non-carbonaceous chondrite affinity (NC) iron meteorites also suggests that planetesimals and planetary embryos in the inner Solar System did not accrete volatile-poor material[9]. Consequently, post-accretion processes should have played an important role in establishing the N- and C-depleted character of the bulk silicate reservoirs of rocky bodies.

Early differentiation processes such as core–mantle separation and atmospheric loss play an important role in explaining N and C depletion in the bulk silicate Earth (BSE)[3,4,10–15]. However, the effect of a differentiated character of the earliest-forming protoplanets on the dynamics of N and C retention and loss during planetary growth is not known. Several lines of evidence point towards a differentiated character of these protoplanets independent of their growth zone: (1) rapid accretion and differentiation of asteroid- and planetary embryo-sized rocky bodies, including parent bodies of carbonaceous chondrite (CC) affinity and NC iron meteorites[16], when ^{26}Al was extant; (2) geochemical evidence for the presence of global magma oceans (MOs) on asteroid-sized Vesta and angrite parent bodies[17]; and (3) palaeomagnetic evidence for the presence of magnetic core dynamos in the parent bodies of CV and CM carbonaceous chondrites which originated in the outer Solar System[18,19]. If differentiation was ubiquitous in the earliest-forming protoplanets at varying heliocentric distances, can it explain the widespread N- and C-depleted character of the bulk silicate reservoirs of all rocky bodies independent of their sizes and the timescales of their growth?

In the earliest-formed protoplanets, large-scale melting by ^{26}Al decay triggered metal–silicate separation as well as volatile degassing[20,21]. Vapour pressure-imposed solubility determines the volatile distribution between the overlying proto-atmosphere and silicate MO and, consequently, the amount of volatiles partitioned into the core. Unlike C, whose concentration in MOs is challenging to determine due to the formation of accessory phases such as graphite, N is an ideal proxy to explore the fate of volatiles during protoplanetary differentiation. This is because the vapour pressure-imposed solubility of N in the silicate melts is controlled by fO_2 and p_N, and $D_N^{alloy/silicate}$ (concentration of N in alloy/concentration of N in silicate) by fO_2 (ref. [11–13]), with much smaller effects of other thermodynamic parameters. $D_N^{alloy/silicate}$ combined with the vapour pressure-imposed N solubility in the silicate melts can thus be used to constrain the coupled N partitioning between all three reservoirs, accounting for the variation in the composition of accreting material as well as the sizes of the protoplanets (Fig. 1).

Partitioning of nitrogen between alloy and silicate melts

$D_N^{alloy/silicate}$ as a function of fO_2 has chiefly been determined in graphite-saturated conditions yielding C-rich alloys containing 3.5–5.5 wt.% C (refs. [10–13,22]). Experiments at ambient[23] and high pressure[24] have shown that C has a strong negative effect on N dissolution in Fe,Ni alloys because N and C occupy similar interstitial voids in the alloy melt structure. As typical core-forming alloys are not expected to be graphite saturated[14], previous experimental studies might have underestimated $D_N^{alloy/silicate}$ if similar negative interactions between N and C persist for P–T–fO_2 conditions relevant for protoplanetary and planetary core–mantle differentiation. Some data from ref. [15] in a limited fO_2 range support this hypothesis but remain unquantifiable (see Methods). It is also unknown whether the effect of

[1]Department of Earth, Environmental, and Planetary Sciences, Rice University, Houston, TX, USA. [2]St. John's School, Houston, TX, USA.
✉e-mail: dsg10@rice.edu

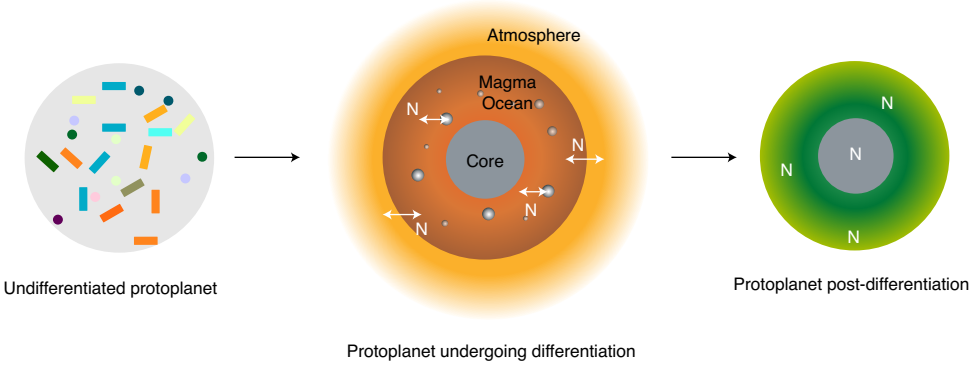

Fig. 1 | The fate of nitrogen during protoplanetary differentiation. An undifferentiated protoplanet represents an amalgamation of primitive chondrite-like material. Heat released during the decay of ^{26}Al causes large-scale melting which triggers metal–silicate separation as well as volatile degassing[20,21,45]. The vapour pressure-induced solubility sets N abundances in the overlying atmosphere and magma ocean, and consequently the amount of N partitioned into the core via equilibrium exchange between magma ocean–core–atmosphere reservoirs. Post-differentiation, N retained in the silicate and metallic reservoirs is only available during subsequent stages of planetary growth while the proto-atmospheres are lost either due to the inability of the smaller bodies to retain their atmospheres or due to impact-induced erosion.

C content in alloy on $D_N^{alloy/silicate}$ persists across the wide fO_2 range applicable for protoplanetary and planetary differentiation.

To constrain $D_N^{alloy/silicate}$ in graphite-undersaturated conditions, we performed piston cylinder experiments using Fe-Ni-N±Si alloys and silicate mixtures in MgO capsules at 3 GPa and 1600–1800 °C (Supplementary Table 1). The rationale for the chosen experimental conditions is based on previous studies[10–13,22] which showed that $D_N^{alloy/silicate}$ is primarily controlled by fO_2 with P having a minimal effect for alloy–silicate equilibration in planetesimals and planetary embryos[11,12,15]. Reaction of silicate mixtures with MgO capsules generated ultramafic silicate melts that better represent planetary MO compositions (Extended Data Fig. 1). To cover the compositional range for protoplanets accreted at disparate heliocentric distances, the experiments covered a wider fO_2 range (from IW–7.10 to IW–1.54, where IW refers to the fO_2 set by equilibrium co-existence of iron (Fe) and wüstite (FeO); Supplementary Table 2) in comparison with previous studies (IW–4.20 to –0.07; refs. [10–13,15,22]). A time series conducted between 0.5 and 12 h demonstrates minimal variations in N contents in alloy and silicate melts as well as silicate melt compositions with time (Extended Data Fig. 2 and Methods). Also, there was no zonation of N content in either alloy melt or silicate phases. Collectively, these results demonstrate that the experiments had reached equilibrium at less than 0.5 h. Therefore, a runtime of 45 min to 3 h (comparable to previous studies in graphite-saturated conditions[10–13]) was deemed sufficient to determine equilibrium $D_N^{alloy/silicate}$ values. Experimental products comprised metal blobs embedded either in silicate glass (Fig. 2a) or in a matrix of silicate glassy pools along with quenched dendritic crystals (Fig. 2b), fine quenched crystals (Fig. 2c) or euhedral olivine (Fig. 2d), and periclase. N and other major and minor element abundances in alloy and glassy melts were determined using electron microprobe analysis (Supplementary Tables 3 and 4 and Methods). Only N-H peak was observed spectroscopically in the silicate glasses (Extended Data Fig. 3 and Methods). In experiments comprising both glassy and quenched crystal domains, the N content in the glassy pools was used to estimate the N concentration of the silicate melt because the dendritic matte that forms during quenching results in loss of N due to melt compaction[11].

C contents in graphite-undersaturated alloy melts of this study vary between 0.11 and 0.80 wt.% and are substantially lower than the values for graphite-saturated alloys reported in previous studies (3.5–5.5 wt.%) (Extended Data Fig. 4a). Even though the starting mixtures were nominally C free, atmospheric contamination during

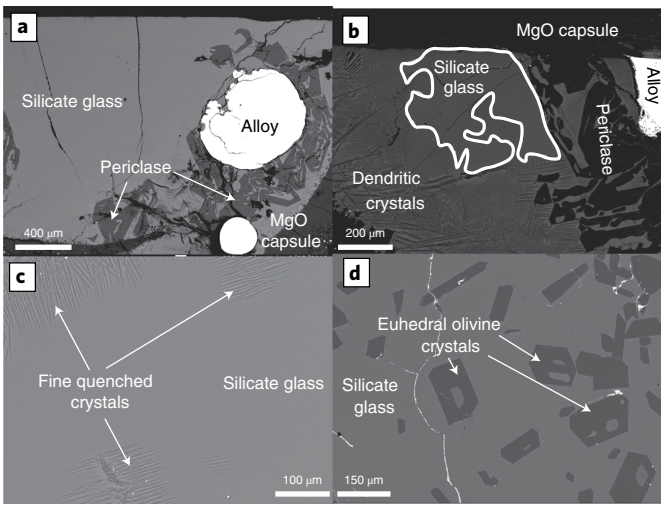

Fig. 2 | Back-scattered electron images of experimental products. a, Co-existence of quenched alloy blobs and silicate glass with periclase in MgO capsule (G608; 3 GPa, 1,700 °C, IW–6.62). **b**, Co-existence of quenched alloy blobs with silicate glass pools, dendritic olivine crystals and periclase (X25; 3 GPa, 1,600 °C, IW–3.51). **c**, Texture of silicate glass co-existing with fine quenched crystals (X39; 3 GPa, 1,700 °C, IW–4.60). **d**, Texture of silicate glass co-existing with euhedral olivine crystals (X43; 3 GPa, 1,800 °C, IW–4.22).

preparation and/or diffusion of carbon from the graphite heater during the experiments could have been the potential source of C in the alloy melts. In agreement with graphite-saturated experiments[11], the N content in the alloy decreases with decreasing fO_2, followed by a sharp drop at ~IW–4, caused by incorporation of Si into the alloy melt (Extended Data Fig. 4b). This drop results from an increase in $\gamma_N^{alloy\ melt}$ (activity coefficient of N in the alloy melt with infinitely dilute solution as the standard state) with increasing Si due to non-ideal interactions between Si and N (Fig. 3a). At a given fO_2, N contents are higher in graphite-undersaturated alloys by a factor of ~2–10 relative to graphite-saturated alloys (Extended Data Fig. 4b). $\gamma_N^{alloy\ melt}$ for Si-free alloys increases from ~1 for graphite-undersaturated alloys to ~3–4 for graphite-saturated alloys at a fixed fO_2 (Fig. 3a). This confirms that negative

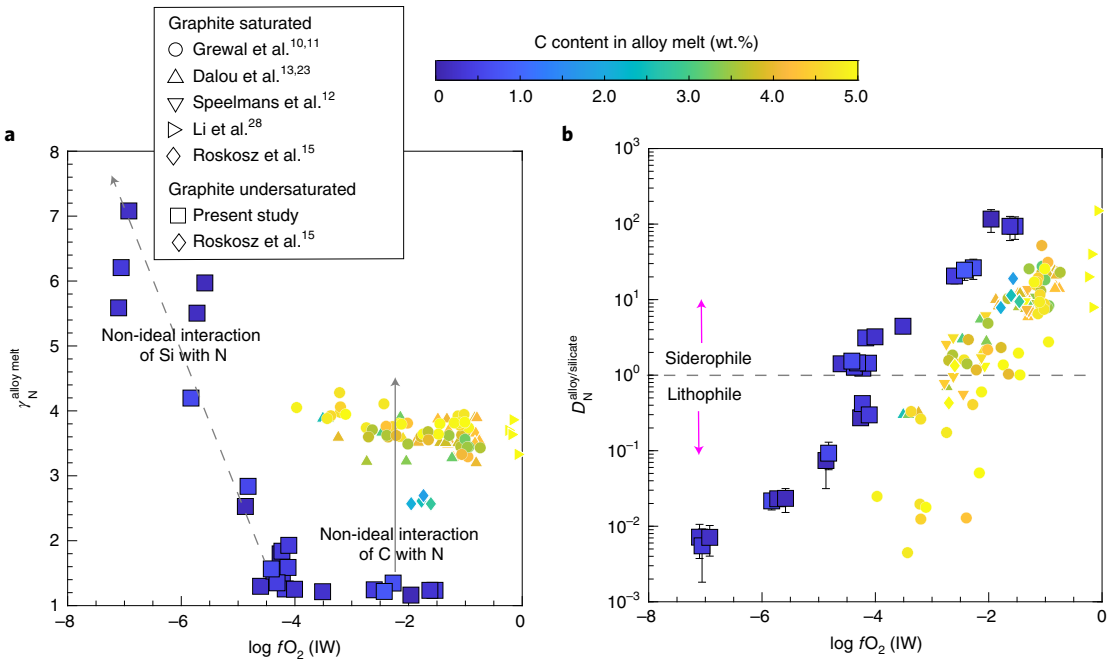

Fig. 3 | $\gamma_N^{alloy\ melt}$ and $D_N^{alloy/silicate}$ as functions of oxygen fugacity and carbon content in the alloy melt. a, $\gamma_N^{alloy\ melt}$ in C-poor and Si-free alloy melts in this study is ~1, while $\gamma_N^{alloy\ melt}$ is ~3–4 at similar fO_2 for graphite-saturated alloys. This is due to non-ideal interactions between C and N occupying similar octahedral voids in the alloy melt. Higher $\gamma_N^{alloy\ melt}$ for C-poor and Si-bearing alloys results from repulsive interactions between Si and N. **b**, In agreement with previous studies in graphite-saturated conditions[10–13,22,27], $D_N^{alloy/silicate}$ decreases with decreasing fO_2 in graphite-undersaturated conditions. At any given fO_2, $D_N^{alloy/silicate}$ in graphite-undersaturated conditions is almost an order of magnitude higher relative to graphite-saturated conditions. $\gamma_N^{alloy\ melt}$ was calculated using the Online Metal Activity Calculator (http://norris.org.au/expet/metalact/), which uses the ε approach via Wagner equations. Error bars for $D_N^{alloy/silicate}$ represent ±1σ deviation obtained by propagation of ±1σ deviation on the N content in the alloy and silicate melts; where absent, the error bars are smaller than the symbol size.

interactions between N and C also persist at high *P*–*T* conditions relevant for protoplanetary differentiation and indicates that N dissolution in core-forming alloy melts was severely underestimated using graphite-saturated alloys. Consequently, at any given fO_2, $D_N^{alloy/silicate}$ for graphite-undersaturated alloys is nearly an order of magnitude higher than that for graphite-saturated alloys (Fig. 3b). N acts as a siderophilic element over a wider fO_2 range (>~IW–4.5) in graphite-undersaturated conditions relative to graphite-saturated conditions (>~IW–2). The decrease in $D_N^{alloy/silicate}$ with decreasing fO_2 is due to an increase in $\gamma_N^{alloy\ melt}$ and the stability of N^{3-} in the silicate melt[25,26] under extremely reducing conditions. Also, we find that, at a similar log fO_2 (~IW–4), incorporation of Si into the alloy melt decreases $D_N^{alloy/silicate}$ substantially (Extended Data Fig. 5a). In contrast to previous studies, $D_N^{alloy/silicate}$ does not vary with *T* (Extended Data Fig. 5b). The experimental analyses show that ~50–85% of N was recovered in the final products (Extended Data Fig. 6). This lies within the range of or is higher than the N recovery in graphite capsules[10–13,22,27]. The lack of correlation between N loss and $D_N^{alloy/silicate}$ and the correlations of $D_N^{alloy/silicate}$ with other thermodynamic parameters (for example, fO_2 and C content of alloy) suggest adherence to Henry's law.

Alloy–silicate–atmosphere fractionation of nitrogen

The fate of N during protoplanetary differentiation depends on the growth rate and final sizes of protoplanets that formed within ~1–2 Myr of Ca–Al-rich inclusion (CAI) formation as well as their chemical compositions (tracked here by fO_2). Numerical and cosmochemical models predict an almost instantaneous accretion of Vesta-sized asteroids and Moon- to Mars-sized planetary embryos within ~0.1–2 Myr of CAI formation[28–31]. Even though smaller planetesimals were more numerous, most of the mass was distributed in asteroid- and planetary embryo-sized bodies[29,30]. To account for variation in the sizes of protoplanets, we assume four end-members cases: Vesta ($R \approx 250$ km, $0.04R_\oplus$, $0.00004M_\oplus$), an intermediate-sized hypothetical protoplanet ($R \approx 750$ km, $0.12R_\oplus$, $0.001M_\oplus$), the Moon ($R \approx 1{,}740$ km; $0.27R_\oplus$, $0.012M_\oplus$) and Mars ($R \approx 2{,}440$ km; $0.53R_\oplus$, $0.107M_\oplus$, where $R_\oplus$ and $M_\oplus$ are the radius and mass of the present-day Earth, respectively). Once a rocky body grew rapidly to its final size[28–30], it is assumed to have undergone global melting leading to the formation of an MO (via heat released by ^{26}Al decay) overlain by a degassed atmosphere[20,21] (Fig. 1). Vapour pressure-induced solubility sets the N content in the MO, which in turn determines the availability of N to partition into core-forming alloy. Alloy–silicate equilibration sets the fO_2 of the MO. The effect of the compositional gradient of the accreting material is accounted for by alloy–silicate equilibration at different fO_2. It is important to note that differentiation at log fO_2 > IW–4 is representative for most rocky bodies in the Solar System and only Mercury and the aubrite parent body underwent differentiation at more reducing conditions (log fO_2 < IW–5)[32] (Fig. 4b). As alloy–silicate equilibration was extremely efficient in planetesimal- and planetary embryo-sized bodies[33], complete alloy–silicate melt equilibration was assumed. N abundances in the atmosphere, MO, and alloy melts are calculated simultaneously using parameterized N solubility equation from ref. [25] and the parameterized $D_N^{alloy/silicate}$ equation from this study (Eq. 3; Supplementary Table 5 and Extended Data Fig. 7).

The distribution of N between the atmosphere, MO, and core reservoirs as a function of fO_2 for end-member protoplanets is shown

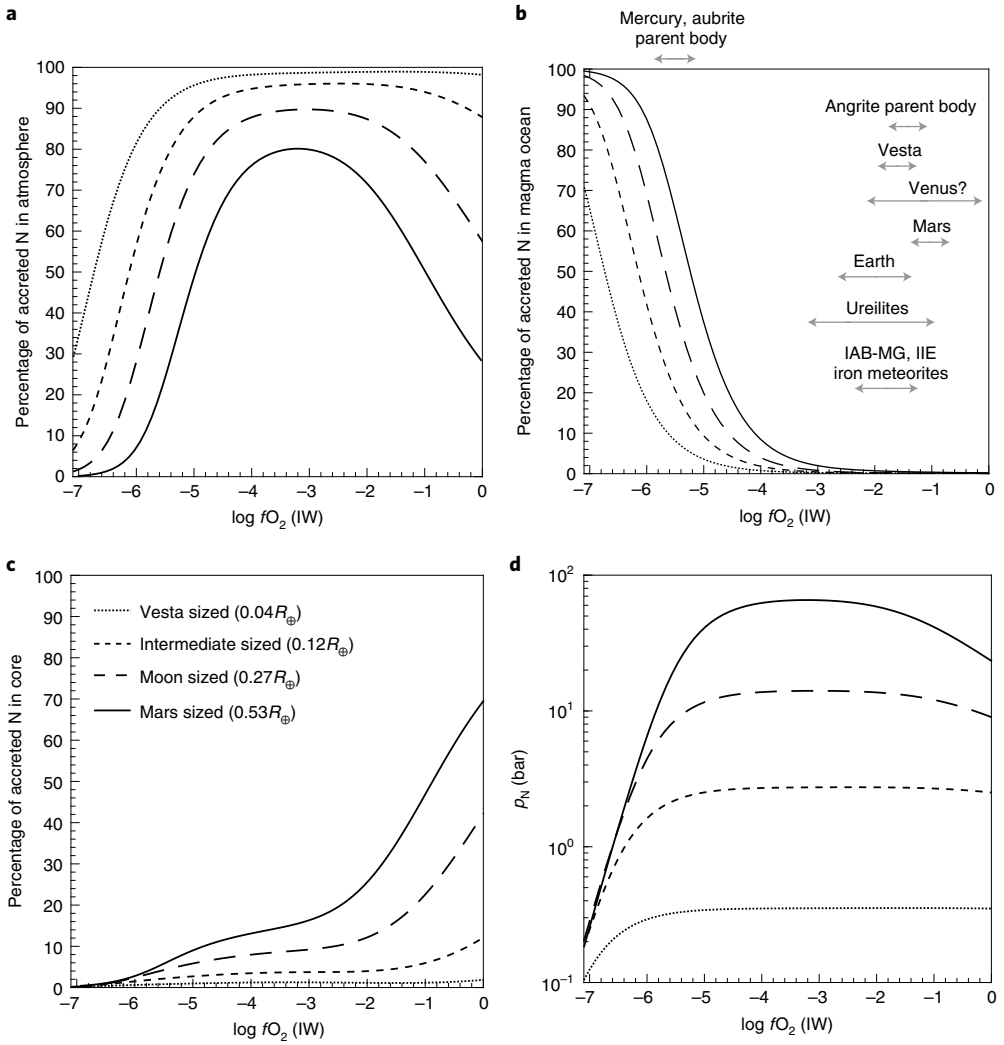

Fig. 4 | Relative distribution of nitrogen in constituent reservoirs of protoplanetary bodies as a function of oxygen fugacity. a–d, At any given fO_2, the proportion of N in the atmospheric reservoir (**a**) decreases, while it increases in the magma ocean (**b**) and core reservoir (**c**) with increase in the size of the rocky body. Assuming these bodies had similar densities, their N partial pressures (p_N) correlate with their radii. Therefore, large bodies have higher p_N (**d**), resulting in a higher amount of N dissolving into their MOs and cores. As the N solubility in the MO decreases and the siderophilic character of N increases with increasing fO_2, the proportion of N in the MO decreases and the proportion of N in the atmosphere and/or core increases. Consequently, for rocky body differentiation at log fO_2 > IW–4, asteroid-sized (Vesta (0.04$R_\oplus$) and intermediate-sized (0.12$R_\oplus$)) bodies have almost all of their N in the atmospheric reservoir, while for planetary embryo-sized bodies (Moon (0.27$R_\oplus$) and Mars (0.53$R_\oplus$)) the cores become an important reservoir for N storage. The oxygen fugacities of core–mantle differentiation of rocky bodies in **b** are compiled in Supplementary Table 6.

in Fig. 4 for a fixed alloy/silicate mass ratio ($r = 0.5$; Earth's alloy/silicate ratio), a bulk N content of 500 ppm (within the range of carbonaceous and enstatite chondrites[8]) and alloys having 0–0.4 wt.% C (the estimated upper limit for the C content of Earth's core[4]). The distribution of N within different reservoirs depends on a complex interplay between the N solubility in MO and $D_N^{alloy/silicate}$, which directly depends on the size of the body and the fO_2 of the accreting material. At any given fO_2, the percentage of N in the atmospheric reservoir decreases with increase in the size of the rocky body (Fig. 4a). Therefore, a Vesta-sized protoplanet has almost all of its N inventory in the atmospheric reservoir (except below IW–5), while larger protoplanets have proportionally lesser N (Fig. 4a). Assuming that the density of the material accreted by protoplanets was similar, p_N scales as a function of radius (R) and gravitational constant (g) such that larger bodies have higher p_N at a given fO_2 (Fig. 4d). Hence, more N dissolves into the MOs of larger bodies at a fixed fO_2 (Fig. 4b). Consequently, a greater amount of N is available for fractionation between MO and alloy melts, allowing a higher proportion of N to segregate into the cores of larger bodies at a given fO_2 (Fig. 4c). For all rocky bodies, N in the atmospheric reservoir increases from IW–7 to IW–4 because the N solubility in the MO drops with increase in fO_2 and the core cannot incorporate substantial amounts of N due to $D_N^{alloy/silicate}$ being lower than 1 under reducing conditions. Above IW–4, N in the atmospheric reservoir decreases (especially for larger bodies) even though its solubility in the MO decreases because N shows an increasingly siderophilic character with increasing fO_2. Accordingly, cores become an important reservoir for N storage in larger protoplanets. For example, cores contain up to ~40% and ~70% of the accreted N budget in Moon- and Mars-sized planetary embryos, respectively. As a result, MOs relevant only for Mercury and the aubrite parent body (log fO_2 < IW–4) retain a substantial fraction of N in their silicate reservoirs. Above log fO_2 > IW–4, the MOs of protoplanets are extremely N depleted (<0.1% of the initial accreted N) irrespective of their

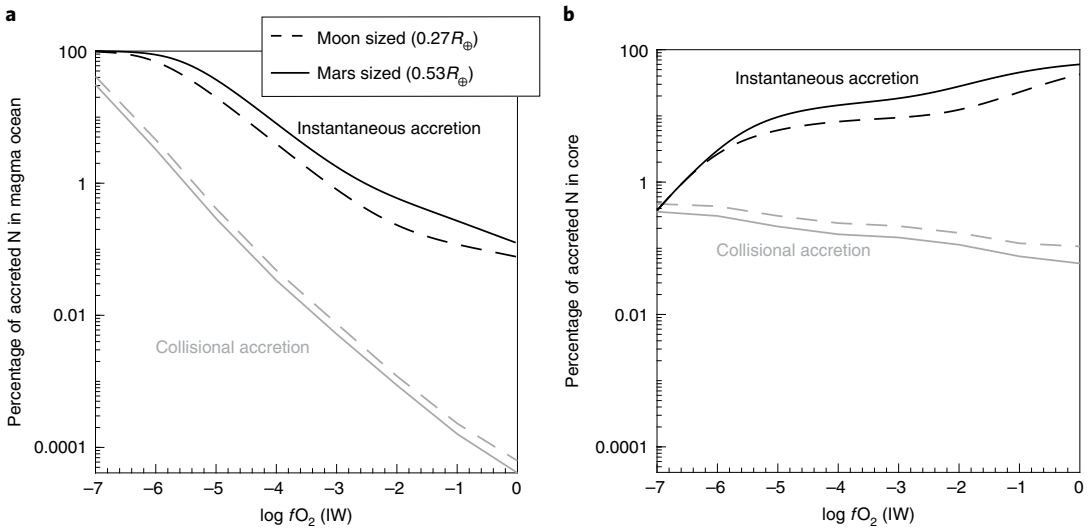

Fig. 5 | Comparison of N distribution in non-atmosphere reservoirs of planetary embryos that grew via either instantaneous or collisional accretion. a,**b**, Planetary embryos that grew via instantaneous accretion and then underwent differentiation have a much higher percentage of initially accreted N in their magma oceans (**a**) and cores (**b**) relative to planetary embryos that grew via collisional accretion of differentiated planetesimals. In this figure, Vesta-sized differentiated bodies (0.04$R_\oplus$) are assumed to be the seeds of collisional accretion leading to Moon- and Mars-sized planetary embryos.

sizes—either solely due to degassing of N into the atmosphere or in combination with N segregating into the cores. Although Moon- to Mars-sized planetary embryos allow vapour pressure buildup leading to substantial volatile in-gassing into MOs and cores[20,34], such vapour pressure build up is unlikely for asteroid-sized bodies due to rapid atmospheric escape as a result of their small gravitational pull[20,21]. Therefore, our predictions for N in the MOs and cores for Vesta- and intermediate-sized bodies represent an upper limit.

Although we assumed fixed bulk N and alloy/silicate mass ratio in Fig. 4, the relative distribution of N during differentiation remains practically unchanged irrespective of the variations in the alloy/silicate mass ratio or the efficiency of alloy–silicate equilibration (Supplementary Fig. 1) and initial amount of accreted N (Supplementary Fig. 2). This suggests that the variation in size of the protoplanets and the composition of their accreting material control the relative distribution of N during protoplanetary differentiation. However, using $D_N^{alloy/silicate}$ determined for graphite-undersaturated alloys is critical for the conclusions drawn in Fig. 4. $D_N^{alloy/silicate}$ is distinctly lower for graphite-saturated systems, which results in the atmosphere being the dominant N-bearing reservoir at log fO_2 > IW–4, irrespective of the size of the parent body (Supplementary Fig. 3).

Rate of protoplanetary accretion versus differentiation

The earliest planetesimals and planetary embryos formed via instantaneous accretion acted as seeds for the planetary embryos and planets that grew later. Therefore, the relative distribution of N between their atmospheric and non-atmospheric reservoirs has important implications for the fate of volatiles during the next stage of planetary growth via planetesimal and planetary embryo collisions. High stellar heating during the protoplanetary disk stage and low escape velocities of the earliest-forming asteroids and planetary embryos makes it improbable that the earliest-formed protoplanets retained their MO degassed atmospheres post differentiation[20,35–37]. Moreover, accretional impacts can lead to complete obliteration of any left-over protoplanetary atmospheres[38]. Therefore, N retained only in their non-atmospheric reservoirs (mantle + core) would be available during subsequent stages of planetary growth. For protoplanets that accreted extremely reduced material such as Mercury and the aubrite parent body, silicate MOs were the prominent N-bearing non-atmospheric reservoir (Fig. 4b). For protoplanets that underwent differentiation at log fO_2 > IW–4, metallic cores were the dominant N-bearing non-atmospheric reservoir (especially for Moon- to Mars-sized planetary embryos). Metallic cores, unlike MOs, are isolated reservoirs after their formation with minimal scope for volatile loss[3]. Thus, the cores can act as the primary N-delivery source for every subsequent stage of planetary growth via partial or complete emulsification of the impactor's core in the target's MO. In contrast to planetary embryos formed by instantaneous accretion (accretion of planetary embryo-sized bodies before undergoing differentiation via heat released by ^{26}Al decay; Fig. 4)[28,29], growth of planetary embryos from differentiated asteroid-sized bodies results in their MO and core reservoirs being extremely N depleted (<0.01% and <0.5% of the initial accreted N inventory, respectively) (Fig. 5 and Methods). Therefore, depending on whether planetary embryos were formed via instantaneous accretion or collisional growth, similar-sized planetary embryos can have very different volatile distribution in their constituent non-atmospheric reservoirs based on their accretion history. Planetary embryos formed via instantaneous accretion contain a substantial amount of N in their silicate and core reservoirs, while planetary embryos formed via collisional growth are extremely N depleted (Fig. 5). Therefore, depending on their accretion history, Moon- to Mars-sized planetary embryos (which acted as seeds for the growth of larger planets such as Earth and Venus via collisional accretion) can have silicate and core reservoirs lying in the range from almost volatile free to volatile bearing.

N in the BSE as a constraint of planetary growth regime

The N budget of the present-day planets can be used to test whether planetary embryo growth via instantaneous or collisional accretion was the dominant mechanism in the Solar System. Earth is the only rocky body with constraints of N abundance in its bulk silicate reservoir[1,39]. Although there is a broad consensus that a large rocky planet such as Earth had a protracted growth history fuelled by the collisional accretion of Moon- to Mars-sized planetary embryos[33,40], the trajectory of its accretionary path is debated. A change in the composition of accreting material from reduced to oxidized as well as oxidized to reduced have been hypothesized to reach the post

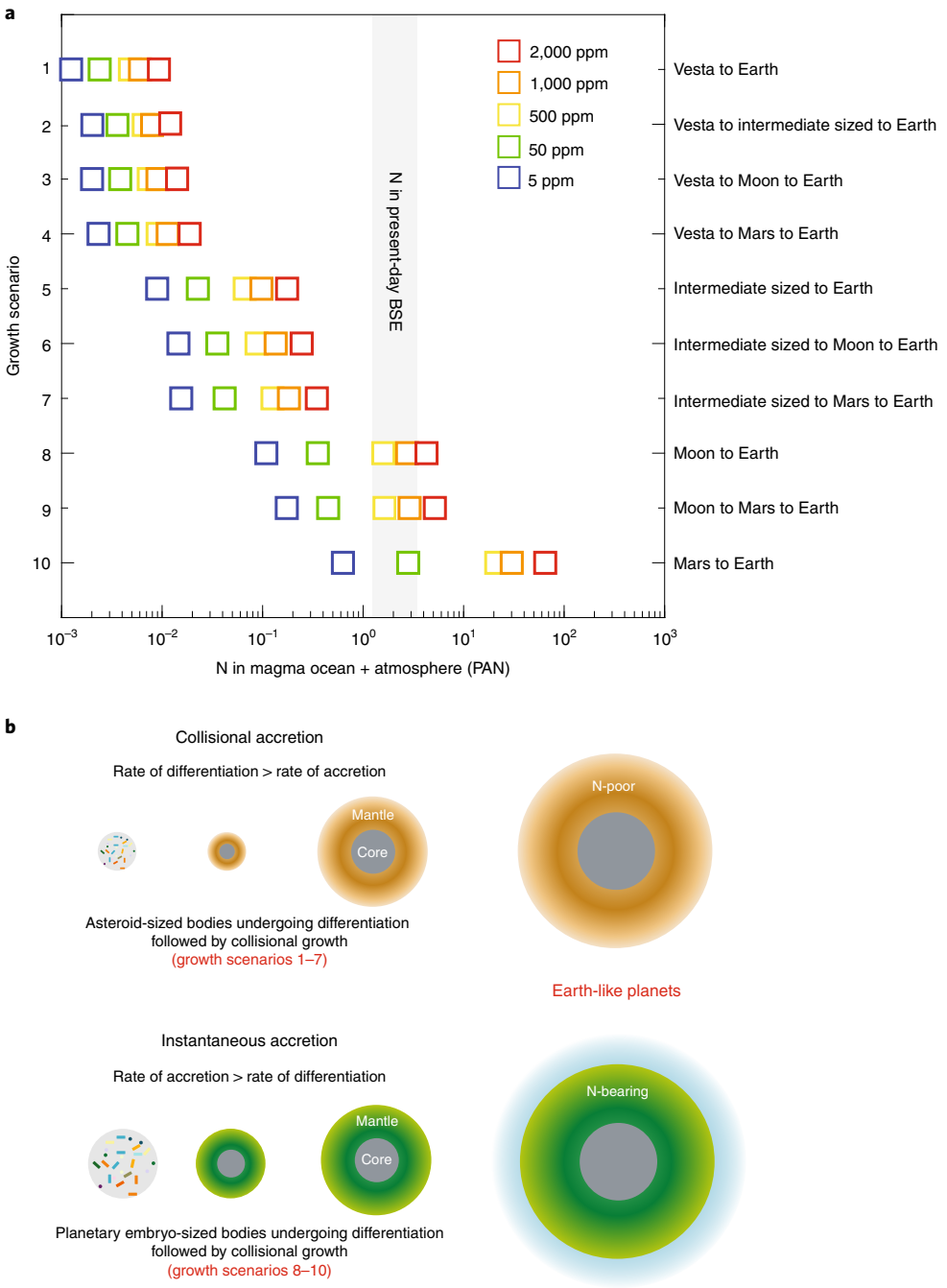

Fig. 6 | Effect of rate of protoplanetary accretion versus differentiation on the nitrogen budget of large Earth-like planets. If the rate of differentiation was greater than the rate of accretion, differentiated asteroid-sized bodies would be the primary building blocks for subsequent stages of growth of larger planets such as Earth. In such cases (scenarios 1–7), the N budget of the BSE cannot be satisfied during the main stage of planetary growth because the mantles and cores of differentiated asteroids were extremely N poor. However, if the rate of accretion was greater than the rate of differentiation, then the N budget of the BSE can be set during the main growth period of Earth via primitive rocky bodies which grew to planetary embryo size before undergoing differentiation (scenarios 8–10). The highest value of accreted N (2,000 ppm) in **a** represents the average N content of volatile-rich CI chondrites[5]. The N abundance in magma ocean + atmosphere in **a** is calculated in terms of the present-day atmospheric nitrogen (PAN) inventory. The right axis in **a** represents end-member growth scenarios of Earth via collisional growth. For example, growth scenario 1 represents Vesta-sized differentiated bodies ($0.04R_{\oplus}$, $0.00004M_{\oplus}$) accreting together to form an Earth-sized planet, and growth scenario 2 represents Vesta-sized differentiated bodies ($0.04R_{\oplus}$) initially accreting to form intermediate-sized rocky bodies ($0.12R_{\oplus}$, $0.001M_{\oplus}$), which subsequently accrete to form an Earth-sized planet. The grey shaded region in **a** represents the estimated N content of the present-day BSE[1,39]. Panel **b** depicts an illustration comparing the N budgets of the bulk silicate reservoirs of Earth-like planets formed from protoplanets having different timescales of accretion and differentiation. Grey, undifferentiated rocky bodies; orange, N-poor differentiated rocky bodies; green, N-bearing differentiated rocky bodies.

core-formation log fO_2 of Earth's primitive mantle, that is, IW–2 (refs. [33,41]). Assuming protoplanetary core–mantle differentiation at IW–2, Fig. 6a shows the effect of different accretion histories of protoplanets on the final N budget of the BSE (see Methods). Accretion of Earth via planetary embryos that accreted from differentiated asteroids (scenarios 1–7) would generate a BSE inventory

containing 0.001–0.4 PAN (Fig. 6a). A superchondritic C/N ratio of the BSE[3,4,10,13] as well as its N isotopic heterogeneity (^{15}N-poor nature of Earth's mantle relative to its atmosphere)[42] suggest that late accretion (post main stage of Earth's growth) of any given class of primitive chondrites cannot explain the present-day N inventory of the BSE post accretion of extremely N-depleted planetary embryos (scenarios 1–7). However, growth of Earth via planetary embryos that underwent instantaneous accretion followed by differentiation (scenarios 8–10) can satisfy the BSE's present-day N budget for 50–1,000 ppm of accreted N (Fig. 6a). For planetary embryos undergoing differentiation at IW–2, the cores contain most of their non-atmospheric N inventory (Fig. 4c); therefore, almost all of the N (>95%) in the target's MO is supplied via emulsification of the impactor's core in the target's MO (see Methods). The efficacy of the retention of atmosphere formed after the last accretion event on Earth (Extended Data Fig. 8a) and the variation in the percentage of emulsification of the impacting planetary embryo's core in the proto-Earth's MO (Extended Data Fig. 8b) only affect the exact amount of accreted N required to satisfy the N content of the present-day BSE but without affecting the broader conclusions.

If the present-day N budget of the BSE was set during the main growth stage of Earth, then the rate of accretion of Moon- to Mars-sized planetary embryos was greater than their rate of differentiation such that planetary embryo-sized protoplanets accreted extremely early, that is, within decay timescales of ^{26}Al (Fig. 6b). Rapid accretion of planetary embryos followed by their differentiation may deplete N to an extent such that enough N is still available to satisfy the N budget of large rocky planets during the later stages of planetary growth via collisional accretion. Rapid growth of planetary embryos is in agreement with pebble accretion models and geochemical estimates of accretion of Moon- to Mars-sized planetary embryos within ~0.1–2 Myr after the formation of CAIs[28,30,31,43]. This means that the origin of N in large Earth-like planets was linked to the growth rates of protoplanets and the amount of N segregated into their cores.

In summary, we show that protoplanetary differentiation can explain the widespread depletion of N in the bulk silicate reservoirs of rocky bodies ranging from asteroids to planetary embryos. Parent body processes rather than nebular processes were responsible for the N- (and possibly C-) depleted character of the bulk silicate reservoirs of rocky bodies in the inner Solar System. A competition between rates of accretion versus rates of differentiation defines the N inventory of bulk planetary embryos and, consequently, larger planets. The N budget of large planets with protracted growth histories can be satisfied if they accreted planetary embryos that grew via instantaneous accretion (Fig. 6b). Because most of the N in those planetary embryos resides in their metallic portions, the cores were the predominant delivery reservoirs for N and other siderophilic volatiles such as C. Establishing the N budget of the BSE chiefly via the cores of differentiated planetary embryos from inner and outer Solar System reservoirs[9] obviates the need for late accretion of chondritic materials as the mode of N delivery to Earth. Also, a siderophilic character of N and C suggests that their accretional pathways in the inner Solar System planets may be decoupled from that of water, which likely accreted from chondritic materials[1,44].

Online content

Any methods, additional references, Nature Research reporting summaries, source data, extended data, supplementary information, acknowledgements, peer review information; details of author contributions and competing interests; and statements of data and code availability are available at https://doi.org/10.1038/s41561-021-00733-0.

Received: 2 April 2020; Accepted: 10 March 2021;
Published online: 10 May 2021

References

1. Marty, B. The origins and concentrations of water, carbon, nitrogen and noble gases on Earth. *Earth Planet. Sci. Lett.* **313–314**, 56–66 (2012).
2. Alexander, C. M. O. The origin of inner solar system water. *Philos. Trans. R. Soc. A* **375**, 20150384 (2017).
3. Hirschmann, M. M. Constraints on the early delivery and fractionation of Earth's major volatiles from C/H, C/N, and C/S ratios. *Am. Mineral.* **101**, 540–553 (2016).
4. Dasgupta, R. & Grewal, D. S. in *Deep Carbon: Past to Present* (eds Orcutt, B. et al.) 4–39 (Cambridge Univ. Press, 2019); https://doi.org/10.1017/9781108677950.002
5. Alexander, C. M. O., McKeegan, K. D. & Altwegg, K. Water reservoirs in small planetary bodies: meteorites, asteroids, and comets. *Space Sci. Rev.* **214**, 36 (2018).
6. Albarède, F. Volatile accretion history of the terrestrial planets and dynamic implications. *Nature* **461**, 1227–1233 (2009).
7. Dauphas, N. The isotopic nature of the Earth's accreting material through time. *Nature* **541**, 521–524 (2017).
8. Grady, M. M. & Wright, I. P. Elemental and isotopic abundances of carbon and nitrogen in meteorites. *Space Sci. Rev.* **106**, 231–248 (2003).
9. Grewal, D. S., Dasgupta, R. & Marty, B. A very early origin of isotopically distinct nitrogen in inner Solar System protoplanets. *Nat. Astron.* https://doi.org/10.1038/s41550-020-01283-y (2021).
10. Grewal, D. S., Dasgupta, R., Sun, C., Tsuno, K. & Costin, G. Delivery of carbon, nitrogen, and sulfur to the silicate Earth by a giant impact. *Sci. Adv.* **5**, eaau3669 (2019).
11. Grewal, D. S. et al. The fate of nitrogen during core–mantle separation on Earth. *Geochim. Cosmochim. Acta* **251**, 87–115 (2019).
12. Speelmanns, I. M., Schmidt, M. W. & LiebskSpeelae, C. The almost lithophile character of nitrogen during core formation. *Earth Planet. Sci. Lett.* **510**, 186–197 (2019).
13. Dalou, C., Hirschmann, M. M., von der Handt, A., Mosenfelder, J. & Armstrong, L. S. Nitrogen and carbon fractionation during core–mantle differentiation at shallow depth. *Earth Planet. Sci. Lett.* **458**, 141–151 (2017).
14. Keppler, H. & Golabek, G. Graphite floatation on a magma ocean and the fate of carbon during core formation. *Geochem. Perspect. Lett.* **11**, 12–17 (2019).
15. Roskosz, M., Bouhifd, M. A., Jephcoat, A. P., Marty, B. & Mysen, B. O. Nitrogen solubility in molten metal and silicate at high pressure and temperature. *Geochim. Cosmochim. Acta* **121**, 15–28 (2013).
16. Kruijer, T. S. et al. Protracted core formation and rapid accretion of protoplanets. *Science* **344**, 1150–1154 (2014).
17. Greenwood, R. C., Franchi, I. A., Jambon, A. & Buchanan, P. C. Widespread magma oceans on asteroidal bodies in the early Solar System. *Nature* **435**, 916–918 (2005).
18. Carporzen, L. et al. Magnetic evidence for a partially differentiated carbonaceous chondrite parent body. *Proc. Natl Acad. Sci. USA* **108**, 6386–6389 (2011).
19. Cournede, C. et al. An early solar system magnetic field recorded in CM chondrites. *Earth Planet. Sci. Lett.* **410**, 62–74 (2015).
20. Young, E. D. et al. Near-equilibrium isotope fractionation during planetesimal evaporation. *Icarus* **323**, 1–15 (2019).
21. Hin, R. C. et al. Magnesium isotope evidence that accretional vapour loss shapes planetary compositions. *Nature* **549**, 511–527 (2017).
22. Dalou, C. et al. Redox control on nitrogen isotope fractionation during planetary core formation. *Proc. Natl Acad. Sci. USA* **116**, 14485–14494 (2019).
23. Jang, J.-M. et al. Nitrogen solubility in liquid Fe-C alloys. *ISIJ Int.* **54**, 32–36 (2014).
24. Liu, J. et al. Loss of immiscible nitrogen from metallic melt explains Earth's missing nitrogen. *Geochem. Perspect. Lett.* **11**, 18–22 (2019).
25. Libourel, G., Marty, B. & Humbert, F. Nitrogen solubility in basaltic melt. Part I. Effect of oxygen fugacity. *Geochim. Cosmochim. Acta* **67**, 4123–4135 (2003).
26. Grewal, D. S., Dasgupta, R. & Farnell, A. The speciation of carbon, nitrogen, and water in magma oceans and its effect on volatile partitioning between major reservoirs of the Solar System rocky bodies. *Geochim. Cosmochim. Acta* **280**, 281–301 (2020).
27. Li, Y., Marty, B., Shcheka, S., Zimmermann, L. & Keppler, H. Nitrogen isotope fractionation during terrestrial core-mantle separation. *Geochemical Perspect. Lett.* 138–147 (2016); https://doi.org/10.7185/geochemlet.1614
28. Weidenschilling, S. J. Accretion of the asteroids: implications for their thermal evolution. *Meteorit. Planet. Sci.* **54**, 1115–1132 (2019).
29. Weidenschilling, S. J. Initial sizes of planetesimals and accretion of the asteroids. *Icarus* **214**, 671–684 (2011).
30. Johansen, A., Low, M. M., Mac, Lacerda, P. & Bizzarro, M. Growth of asteroids, planetary embryos, and Kuiper Belt objects by chondrule accretion. *Sci. Adv.* **1**, e1500109 (2015).

31. Schiller, M., Bizzarro, M. & Fernandes, V. A. Isotopic evolution of the protoplanetary disk and the building blocks of Earth and the Moon. *Nature* **555**, 501–510 (2018).
32. Righter, K., Sutton, S. R., Danielson, L., Pando, K. & Newville, M. Redox variations in the inner solar system with new constraints from vanadium XANES in spinels. *Am. Mineral.* **101**, 1928–1942 (2016).
33. Rubie, D. C. et al. Accretion and differentiation of the terrestrial planets with implications for the compositions of early-formed Solar System bodies and accretion of water. *Icarus* **248**, 89–108 (2015).
34. Elkins-Tanton, L. T. Linked magma ocean solidification and atmospheric growth for Earth and Mars. *Earth Planet. Sci. Lett.* **271**, 181–191 (2008).
35. Zahnle, K. J. & Catling, D. C. The cosmic shoreline: the evidence that escape determines which planets have atmospheres, and what this may mean for Proxima Centauri B. *Astrophys. J.* **843**, 122 (2017).
36. Johnsone, C. P. The influences of stellar activity on planetary atmospheres. *Proc. Int. Astron. Union* **12**, 168–179 (2016).
37. Odert, P. et al. Escape and fractionation of volatiles and noble gases from Mars-sized planetary embryos and growing protoplanets. *Icarus* **307**, 327–346 (2018).
38. Schlichting, H. E., Sari, R. & Yalinewich, A. Atmospheric mass loss during planet formation: the importance of planetesimal impacts. *Icarus* **247**, 81–94 (2015).
39. Hirschmann, M. M. Comparative deep Earth volatile cycles: the case for C recycling from exosphere/mantle fractionation of major (H_2O, C, N) volatiles and from H_2O/Ce, CO_2/Ba, and CO_2/Nb exosphere ratios. *Earth Planet. Sci. Lett.* **502**, 262–273 (2018).
40. Chambers, J. E. & Wetherill, G. W. Making the terrestrial planets: *N*-body integrations of planetary embryos in three dimensions. *Icarus* **136**, 304–327 (1998).
41. Siebert, J., Badro, J., Antonangeli, D. & Ryerson, F. J. Terrestrial accretion under oxidizing conditions. *Science* **339**, 1194–1197 (2013).
42. Cartigny, P. & Marty, B. Nitrogen isotopes and mantle geodynamics: the emergence of life and the atmosphere–crust–mantle connection. *Elements* **9**, 359–366 (2013).
43. Johansen, A. et al. A pebble accretion model for the formation of the terrestrial planets in the Solar System. *Sci. Adv.* **7**, eabc0444 (2021).
44. Piani, L. et al. Earth's water may have been inherited from material similar to enstatite chondrite meteorites. *Science* **369**, 1110–1113 (2020).
45. Hirschmann, M. M. Magma ocean influence on early atmosphere mass and composition. *Earth Planet. Sci. Lett.* **341–344**, 48–57 (2012).

Methods

Starting materials. The starting materials were composed of ~70 wt.% silicate and ~30 wt.% alloy mixtures. A TiO_2-free synthetic tholeiite basalt mixture (ThB1), with identical composition to the silicate mixture of two previous alloy–silicate partitioning studies for N (refs. [10,11]), was used. The silicate starting mixture was made from reagent-grade oxides (SiO_2, Fe_2O_3, Al_2O_3, Cr_2O_3, MnO and MgO) and carbonates ($CaCO_3$, Na_2CO_3 and K_2CO_3). The oxides and carbonates were ground and mixed under ethanol in an agate mortar for ~1.5–2 h. A CO-CO_2 Deltech gas mixing furnace was used to fire the starting silicate mixture at 1,000 °C and ~FMQ–2 (where FMQ refers to the log fO_2 of fayalite–magnetite–quartz buffer) for 24 h to devolatilize the mixture and reduce Fe_2O_3 to FeO. The alloy mixtures were composed of reagent-grade Fe and Ni metals. Si_3N_4 was used as the N source. Variable amounts of Si were added to the starting alloy mixture to simulate increasingly reduced conditions. The alloy mixture was homogenized under ethanol for ~30 min in an agate mortar followed by drying in a desiccator for >2 days. Alloy–silicate mixtures were mixed in 30:70 ratio under ethanol in an agate mortar for ~1 h followed by storage in a desiccator for ~1 day.

High pressure (*P*)/temperature (*T*) experiments. The experiments were performed in MgO capsules at a fixed pressure ($P = 3$ GPa) and three different temperatures (1,600, 1,700 and 1,800 °C) for a given fO_2. All experiments were performed using an end-loaded piston cylinder device at Rice University. The experiments employed a 0.5-inch $BaCO_3$/crushable MgO assembly with straight-walled graphite heaters following the calibrations and procedures detailed in a previous study[46]. Temperature was monitored and controlled by a type C (W5%Re/W26%Re) thermocouple. The experiments were pressurized to the target pressure at room temperature before being heated at a rate of 100 °C min^{-1}. Each experiment was prepared by sintering overnight at ~850 °C before heating to the target temperature. The experiments were brought to room temperature within ~10–20 s by cutting power to the heater. The recovered samples were cut longitudinally using a W-wire saw, mounted in Crystalbond, ground using 1,200-grit sandpaper and polished using 0.3-micron alumina slurry on a velvet cloth. Crystalbond was removed from the samples by soaking in acetone overnight. The polished samples were analysed for N and other major and minor elements using an electron microprobe.

Demonstration of equilibrium. We performed a time series at 3 GPa and 1,600 °C for 0.5, 2, 6 and 12 h to demonstrate that the N content in the alloy and silicate melts as well as the silicate melt composition had attained steady state in our experimental products. Extended Data Fig. 2 shows minimal variations in the N contents of both alloy and silicate melts as well as silicate melt compositions with time for a given starting mixture. This demonstrates that the experiments at 1,600 °C had reached equilibrium at less than 0.5 h. Higher-temperature experiments (1,700 and 1,800 °C) are expected to attain equilibrium at even shorter timescales. Because N diffuses fast at high T (ref. [47]) and based on our time series experiments, the experimental durations of 45–180 min were deemed sufficient. These experimental durations are comparable to or longer than previous experimental studies on C alloy–silicate partitioning experiments in MgO capsules[48,49] and N alloy–silicate partitioning experiments in graphite capsules[10–13].

Texture of quenched products. All experimental products were composed of either metal blobs embedded in homogeneous silicate glass (Fig. 2a) or metal blobs in a matrix of silicate glass pools and quenched dendritic olivine crystals (Fig. 2b). All experiments also had ferropericlase crystals along the capsule wall. Some ferropericlase was also dispersed within the silicate melt or adjacent to the metallic blobs (Fig. 2a,b). A few experiments also showed the presence of euhedral olivine crystal dispersed in the silicate melt (Fig. 2d). As reported in previous studies[12,50], we observed micron-sized quenched dendritic nitrides in the Fe-Ni alloy melt blobs. No bubbles were observed in either the alloy or silicate phase in any of the experimental products, suggesting that no N was exsolved during quenching. This observation is in agreement with previous studies conducted under similar P–T conditions in graphite capsules with roughly equivalent N content in the starting mixtures[10,11].

Analytical procedures. *Electron probe micro-analysis (EPMA).* Major and minor element abundances in the alloy and silicate phases were measured using a JEOL JXA8530F Hyperprobe EPMA at the Department of Earth, Environmental and Planetary Sciences at Rice University. Following several recent studies[10–13], N in the alloy and silicate phases was also measured using EPMA. The silicate phases were analysed using carbon-coated samples and standards. For the analysis of the alloy phases, samples and standards were freshly aluminium coated during each session. All elements, except N, in the silicate phase were measured using natural glass standards from the Smithsonian Institute and mineral standards from SPI Supply. Characteristic K_α X-ray lines of the elements in the silicate phases were measured using the following standards: Smithsonian glasses for Si, Al, Ca, Mg, Fe, Na, K and P; rutile for Ti, chromite for Cr, rhodonite for Mn and pentlandite for Ni. For alloy phase analysis, the following standards were used: laboratory-synthesized stoichiometric Fe_3C (ref. [51]) for C, natural magnetite for O, synthetic Fe metal for Fe, synthetic Ni metal for Ni, and synthetic Si metal for Si. Similar to two previous studies[10,11], synthetic boron nitride (BN) was used as a standard for measuring N in the silicate phases and laboratory-synthesized iron nitride (Fe_3N) (ref. [10]) was used as a standard to measure N in the alloy phase.

Accounting for the heterogeneity of the quenched products, a beam size of 20 microns was used. To measure N along with other elements, an accelerating voltage of 15 kV and a beam current of 50 nA were used for silicate phase analysis, and an accelerating voltage of 12 kV and a beam current of 80 nA were used for alloy phase analysis. These conditions have been deemed optimum to accurately determine N in the alloy and silicate phases from two previous studies[10,11]. N K_α X-ray counts per second were measured using LDE2 crystal, also following previous studies[10,11].

The counting time for all elements in the silicate phases, except N, was 10 s on peak and 5 s on each background. The counting time for N in the silicate phase was 80 s on peak and 60 s each on upper and lower background, which yielded a detection limit of ~320 ppm. When the measured N for a given silicate phase in the most oxidized experiments was close to or below the detection limit, N was measured with counting times of 150 s on peak and 300 s on each background, resulting in a lower detection limit of ~70 ppm.

A counting time of 10 s on peak and 5 s on each lower and upper background was used to analyse all elements in the alloys except N. A counting time of 80 s per peak and 60 s per each background was used to analyse N. Similar to the N analysis in the silicate melts, if the measured N was close to the detection limit (~320 ppm), then N analysis on those samples was conducted with 150 s counting time on peak and 300 s on each upper and lower background, which lowered the detection limit to ~70 ppm. After every ~30 measurements on samples, the standards were re-analysed to account for the effect of C deposition on samples and standards during analysis. The measured C concentration in the alloy phase was corrected by accounting for C blank in Fe metal as well as any C deposition during an analytical session following the protocol described in previous studies[10,11,49].

EPMA totals for extremely reduced, N-bearing silicate glasses. All experiments conducted at ≤~IW–2.5 yielded sum totals (sum of wt.% of all oxides and elemental N) greater than 100 wt.%, with increasingly reduced experiments having higher deviations from 100 wt.%. Similar observations have been made in two previous studies[11,13] on N partitioning between alloy and silicate melts. The authors in ref. [11] suggested that the issue of anomalously high totals could be circumvented if an andesitic rather than basaltic glass standard is used for analysing the silicate glasses of highly reduced experiments because the polymerization of the silicate matrix of highly reduced experiments is similar to that of more polymerized andesitic silicate glasses. Unlike ref. [11], in which the most reduced experiments were at ~IW–4, the present study explored an even more reducing range (up to ~IW–7.1) and it was found that the issue of anomalously high totals could not be resolved either by using a basaltic, andesitic or rhyolitic glass standard. It has been shown that, under extremely reduced conditions, N replaces O in the silicate melt structure to form Si–N bonds[26,52] . Therefore, counting all of the Si in the silicate melt as SiO_2, overestimates the concentration of SiO_2. Assuming that all of the N is present in the silicate melt structure as Si–N linkage, we re-calculated SiO_2 and the totals of oxides in the silicate melt (represented as SiO_2-corr. and Total-corr. in Supplementary Table 3). However, even after these corrections, the EPMA analytical totals remained higher. Similarly high totals in silicate glasses were observed in an N-free study examining the alloy–silicate partitioning behaviour of C under similarly reduced conditions[53]. As Si–SiO_2 buffer lies in the range of fO_2 where these high totals were observed, SiO_2 may be partially reduced to SiO in those experiments, which might have led to overestimation of the SiO_2 content of the silicate melt, and consequently high totals. Thus, Supplementary Table 3 also provides the probable SiO/SiO_2 ratios needed to attain EPMA analytical totals of 100.

Fourier-transform infrared (FTIR) spectroscopy. FTIR spectra were obtained by using a Thermo Nicolet FTIR spectrometer at the Department of Earth, Environmental and Planetary Sciences of Rice University (Extended Data Fig. 3). The experimental glasses were doubly polished to thickness of 50–250 μm and cleaned with acetone and ethanol before a given analytical session. A digital micrometer (ID-C125EXB Mitutoyo Digimatic Indicator) was used to measure the sample thickness. Liquid nitrogen was used overnight before every analytical session to remove atmospheric gas contamination. Blank backgrounds were collected at the beginning of each spectral analysis. FTIR spectra were collected on at least three to four spots per sample. Each spectrum was obtained in the wavenumber range from 650 to 4,000 cm^{-1} with a resolution of 4 cm^{-1} and 128 scans using a 100 × 100 $μm^2$ spot. The final reported spectra represent the averaged values for each sample.

Only one major peak was found, at ~3,300 cm^{-1}, which has been assigned to N-H species in previous studies[26,54]. However, the possible O-H peak at ~3,550 cm^{-1} was absent, which means that the silicate melts are almost anhydrous. Also, the area under the curve of the N-H peak is small in comparison with the FTIR spectra of reduced, graphite-saturated silicate glasses with distinctly higher abundance of H (see Fig. 2 in ref. [26]). Therefore, dissolution of N as anhydrous N^{3-} is inferred to dominate in the silicate melts of this study[26]. This is confirmed by the observation that, even though the N content in the silicate melts increases with decrease in fO_2,

the N-H peak area does not increase with decreasing fO_2 (Extended Data Fig. 3). It is important to note that there are no detectable peaks of C species in the silicate melts in comparison with the complex C–O–N–H speciation in hydrated silicate melts in graphite-saturated conditions.

Estimation of oxygen fugacity. The oxygen fugacity (fO_2) of the experimental products was determined via the co-existence of Fe-rich alloy melt and silicate melt:

$$FeO^{\text{silicate melt}} = Fe^{\text{alloy melt}} + 1/2O_2 \quad (1)$$

from which the fO_2 value relative to the fO_2 of the iron–wüstite buffer (ΔIW), at a given P–T, is defined by

$$\Delta IW = 2\log\frac{a_{FeO}^{\text{silicate melt}}}{a_{Fe}^{\text{alloy melt}}} = 2\log\frac{X_{FeO}^{\text{silicate melt}}\gamma_{FeO}^{\text{silicate melt}}}{X_{Fe}^{\text{alloy melt}}\gamma_{Fe}^{\text{alloy melt}}} \quad (2)$$

where $a_{FeO}^{\text{silicate melt}}$ is the activity of FeO component in silicate melt and $a_{Fe}^{\text{alloy melt}}$ is the activity of Fe component in alloy melt; $X_{FeO}^{\text{silicate melt}}$ and $\gamma_{FeO}^{\text{silicate melt}}$ is the mole fraction and activity coefficient of FeO component in silicate melt, respectively; $X_{Fe}^{\text{alloy melt}}$ and $\gamma_{Fe}^{\text{alloy melt}}$ is the mole fraction and activity coefficient of Fe component in alloy melt, respectively. Using the non-ideal solution model, fO_2 was calculated assuming a fixed $\gamma_{FeO}^{\text{silicate melt}}$ of 1.5 (ref. [55]). To account for the non-ideal interactions between components of the alloy melt, $\gamma_{Fe}^{\text{alloy melt}}$ was calculated via the ε approach in Wagner equations[56] using the Online Metal Activity Calculator (http://norris.org.au/expet/metalact/).

Comparison with the graphite-undersaturated data of Roskosz et al. (2013). In a previous study[15], at 5–10 GPa and a limited fO_2 range (between IW–2.7 and IW–1.5), order of magnitude higher $D_N^{\text{alloy/silicate}}$ values were reported from laser-heated diamond anvil cell (LHDAC) experiments at graphite-undersaturated conditions in comparison with graphite-saturated systems conducted using multi anvil apparatus[15]. However, the quantitative effects of the C content in alloy on $D_N^{\text{alloy/silicate}}$ could not be determined from that study owing to the unavailability of C content measurements on their alloys. Furthermore, it also remained unknown whether the effect of the C content of alloy on $D_N^{\text{alloy/silicate}}$ persists across the entire fO_2 range (between IW–7 and IW–1)[32] applicable for protoplanetary and planetary differentiation.

Parameterization of $D_N^{\text{alloy/silicate}}$. To predict the alloy–silicate partitioning behaviour of N for a wide range of graphite-undersaturated MO settings, we derived an empirical parameterization for $D_N^{\text{alloy/silicate}}$ using data from this study and previous studies[10–13,15,22,27] by incorporating an additional term for the effect of the variation of the C content in the alloy. We note that this is the first $D_N^{\text{alloy/silicate}}$ parameterization that can be applied for both graphite-undersaturated and graphite-saturated alloys. The 164 experiments used for this parameterization covered the following parameter space: P = 1 to 17.7 GPa, T = 1,400 to 2,577 °C, log fO_2 = IW–7.1 to IW–0.2, S content of alloy from 0 to 32.1 wt.%, Si content of alloy from 0 to 24.6 wt.%, non-bridging oxygens per tetrahedral cation (NBO/T) from 0.4 to 2.5 and C content of alloy from 0.1 wt.% to graphite saturated. The empirical equation is based on thermodynamic considerations detailed in ref. [11].

$$\begin{aligned}\ln D_N^{\text{alloy/silicate}} = {} & a + \tfrac{b}{T} + c\tfrac{P}{T} + d\ln\left(100 - X_S^{\text{alloy}}\right) + e\ln\left(100 - X_S^{\text{alloy}}\right)^2 \\ & + f\ln\left(100 - X_{Si}^{\text{alloy}}\right)^2 + g\ln\left(100 - X_C^{\text{alloy}}\right) + h\ln\left(100 - X_C^{\text{alloy}}\right)^2 \\ & + i\text{NBO/T} + j\ln X_{FeO}^{\text{silicate}}\end{aligned} \quad (3)$$

where P is pressure in GPa, T is temperature in K, $X_{FeO}^{\text{silicate}}$ is the FeO content of the silicate melt in wt.% and the NBO/T term accounts for the effect of the silicate melt composition. The presence of S, Si and, C in the alloy melt is accounted for by the terms $\ln\left(100 - X_S^{\text{alloy}}\right)$, $\ln\left(100 - X_{Si}^{\text{alloy}}\right)$ and $\ln\left(100 - X_C^{\text{alloy}}\right)$, where X_S^{alloy}, X_{Si}^{alloy} and X_C^{alloy} denote the wt.% of S, Si and C in the alloy melt, respectively. The built-in 'regress' function in MATLAB was used to perform regression with an unweighted least-squares minimization scheme. The resulting coefficients and their 1σ uncertainties are presented in Supplementary Table 5. The experimental and predicted data show good agreement (Extended Data Fig. 7a). The experiments from ref. [12] containing high initial TiO_2 were not included in the parameterization because they yielded substantially higher $D_N^{\text{alloy/silicate}}$ values at log fO_2 < ~IW–3 in comparison with the data of refs. [11,13] primarily due to the formation of osbornite (TiN) speckles attached to the metallic alloys[12]. The authors of that study[12] had also noted that the high $D_N^{\text{alloy/silicate}}$ values yielded by those experiments 'are an experimental artifact not representing true partitioning values'. Two experiments (HB01 and HB15) from ref. [22] were not included in the parameterization because of the low analytical totals (<95 wt.%) and anomalously low C contents of their alloy phases relative to similar studies conducted under graphite-saturated conditions.

Extended Data Fig. 7b shows a comparison of the empirical $D_N^{\text{alloy/silicate}}$ parameterization developed in this study for the entire range of C content in the alloy (C-free alloys to graphite saturated) with the $D_N^{\text{alloy/silicate}}$ parameterizations of two previous studies determined in graphite-saturated conditions[11,12]. The $D_N^{\text{alloy/silicate}}$ values predicted for graphite-saturated alloys by the parameterization of this study lie within the range of predicted $D_N^{\text{alloy/silicate}}$ of ref. [11] at log fO_2 > ~IW–4. Below ~IW–4, the predicted $D_N^{\text{alloy/silicate}}$ values of ref. [11] decrease sharply due to the incorporation of even small amounts (<0.5 wt.%) of Si in graphite-saturated alloys, which is not captured by the experiments and parameterization of this study. $D_N^{\text{alloy/silicate}}$ values predicted in graphite-saturated alloys by the parameterization of this study are almost similar to those of ref. [12] across the entire fO_2 range. The predicted $D_N^{\text{alloy/silicate}}$ values for C-free alloys as well as C-poor alloys (0.4 wt.%, a concentration similar to the estimated C content of the Earth's core[4]), in agreement with the experimental dataset of this study (Fig. 2b), are approximately an order of magnitude higher than those for systems with graphite-saturated alloys at log fO_2 > ~IW–4. Below IW–4, the gap between the predicted $D_N^{\text{alloy/silicate}}$ values in graphite-undersaturated and graphite-saturated conditions diminishes because the C solubility in the alloy melt drops with the incorporation of Si under such conditions[11,53]. Below IW–6, the predicted $D_N^{\text{alloy/silicate}}$ values in graphite-undersaturated and graphite-saturated alloy-bearing systems are almost similar because the C solubility in the alloy melt approaches the assumed C content (0.4 wt.%) of graphite-undersaturated alloys.

N redistribution between silicate magma ocean, metallic core and atmosphere. Post large-scale melting, the accreted N is distributed between three major reservoirs in a rocky body: atmosphere, silicate magma ocean (MO) and alloy core. The atmosphere overlaying the MO sets the N abundance in the silicate melts via its vapour pressure-induced solubility. The equilibration of the alloy melt with the MO determines the N inventory of the core of the rocky body.

Using a mass balance, the total mass of N is conserved pre- and post-differentiation:

$$M_N^{\text{tot}} = M_N^{\text{atm}} + M_N^{\text{MO}} + M_N^{\text{core}},$$

where M_N^{tot}, M_N^{atm}, M_N^{MO} and M_N^{core} represent the mass of N in the bulk body, atmosphere, magma ocean and core, respectively.

The concentration of N in a given reservoir is represented by

$$C_N^i = M_N^i/m^i,$$

where C_N^i represents the concentration of N in a given reservoir and m^i represents the mass of that reservoir.

Equilibrium between the alloy and silicate is given by $D_N^{\text{alloy/silicate}} = C_N^{\text{alloy}}/C_N^{\text{silicate}}$. $D_N^{\text{alloy/silicate}}$ is calculated as a function of fO_2 using Eq. 3 of this study. Instead of using a fixed

Henry law's constant to calculate C_N^{silicate}, as done in previous studies[3,4,10], in this study C_N^{silicate} is calculated as a function of fO_2 using the following equation from ref. [25]: $C_N^{\text{silicate}} = 0.06p_N + 5.97{p_N}^{1/2}{fO_2}^{-3/4}$ (Extended Data Fig. 9). The partial pressure of N is given by $p_N = M_N^{\text{atm}}g/A$, where g and A are the gravitational constant and the area of a rocky body or MO surface, respectively (Supplementary Table 7).

Collisional growth of asteroid- and planetary embryo-sized rocky bodies. For collisional growth, the rocky bodies are assumed to grow by accretion of a fixed ratio of the resultant rocky body's mass (that is, seed rocky body's mass/final rocky body's mass) at each stage of accretion. The mass of the target increases via collisional accretion of the impactor (seed rocky body) at every step of growth. For all scenarios of rocky body accretion, each of the impactors is assumed to have been differentiated at a given fO_2 with the N distribution in their resulting reservoirs calculated via the coupled metal–silicate–atmosphere fractionation model. At every step of collisional accretion, we assume: (1) global-scale melting of the target's and impactor's mantles[33,57], (2) complete emulsification of the impactor's core in the target's MO[33,57] and (3) complete loss of the atmospheric reservoirs of both the target and the impactor pre-collision or/and during the impact[37,38]. The total amount of N present in the mantle of the target and the impactor as well as the N present in the impactor's core (assumed to be released into the target's MO post-impact) contribute to the post-impact N budget available for metal–silicate–atmosphere fractionation. The core of the target is assumed to be a non-interacting, isolated reservoir. Post impact, the net silicate MO (equal to the mass of the target's + impactor's mantle) equilibrates with the MO degassed atmosphere (dependent on the vapour pressure-induced solubility). N present in the MO is available to equilibrate with the impactor's core-forming alloy (dependent on $D_N^{\text{alloy/silicate}}$). The N exchange between all three reservoirs is calculated simultaneously by the coupled metal–silicate–atmosphere equilibration model as defined above. Finally, the core-forming metal sinks down to form the net post-merger core. We assume that the N content of the silicate mantle remains unmodified as it crystallizes from the MO stage to form the solid mantle. N in the silicate portion of the post-merger body is available for exchange when it acts as a target for the next stage of collisional growth, while N in its core would remain isolated and N in its atmosphere is lost either during collision or due to the rocky body's inability to retain its resulting atmosphere (applicable to asteroids and small planetary embryos).

Collisional growth of Earth. The growth scenarios are categorized as ten end-member scenarios based on the size of the body that originally underwent differentiation and later collided to form larger bodies with increase in MO depth at every step of accretion: (1) scenarios 1–4: Vesta-sized bodies ($0.04R_{\oplus}$, $0.00004M_{\oplus}$), (2) scenarios 5–7: intermediate-sized bodies ($0.12R_{\oplus}$, $0.001M_{\oplus}$), (3) scenarios 8 and 9: Moon-sized bodies ($0.27R_{\oplus}$, $0.012M_{\oplus}$) and (4) scenario 10: Mars-sized bodies ($0.53R_{\oplus}$, $0.107M_{\oplus}$), where $R_{\oplus}$ and $M_{\oplus}$ are the radius and mass of the present-day Earth, respectively. The collisional growth of Earth follows a similar framework as explained in the previous section. Growth of Earth via accretion of asteroid-sized bodies acting as seeds (scenarios 1–7) would lead to an extremely N-depleted BSE, while growth of Earth via planetary embryo-sized bodies acting as seeds (scenarios 8–10) can satisfy the N budget of the BSE for varying values of net accreted N in the seed planetary embryo (Fig. 6). As described in the previous section, N present in the MO of the target and the impactor as well as N in the impactor's core contribute to the net N available for metal–silicate–atmosphere fractionation. The atmosphere of the target and the impactor are both assumed to be lost either pre-collision or/and stripped away during every stage of collision. However, after the final accretion event on Earth, that is, when Earth has attained almost all of its mass (possibly after the Moon formation event), the final atmosphere formed after the MO degassing is assumed to be retained in the calculations presented in Fig. 6. This is a reasonable assumption as late accretion events after the Moon-forming impact may not be energetic enough to lead to the complete removal of Earth's atmosphere. If there were a substantial amount of atmospheric loss post the last step of accretion, then consistently higher accreted bulk N values would be required. For example, in scenario 10, for 50 ppm of accreted N in Mars-sized planetary embryos that underwent differentiation, ~60–100% atmospheric retention would be enough to satisfy the N budget of the present-day BSE, and for lesser degrees of atmospheric retention higher amounts of bulk accreted N would be required (Extended Data Fig. 8a).

Also, we assumed complete emulsification of the impactor's core in the target's MO after every stage of collision for the results presented in Fig. 6. This is a reasonable assumption for the asteroid-sized bodies as well as Moon-sized planetary embryos[33,57]. However, this assumption may not hold true for relatively large, Mars-sized impactors[58,59]. To account for the effect of inefficient emulsification of the impactor's core in the target's MO, we provide an additional set of example calculations for scenario 10 with 50 ppm of accreted N. Greater than 50% emulsification of the impactor's core in the target's MO during every stage of impact would satisfy the N budget of the present-day BSE if Mars-sized impactors had accreted 50 ppm N. Lesser degrees of emulsification of the impactor's core in the target's MO would require higher amounts of bulk accreted N (Extended Data Fig. 8b).

Data availability

The data supporting the findings of this study are available within the article and its Supplementary Information files. All new data associated with this paper will be made publicly available at https://doi.org/10.6084/m9.figshare.14191079.

References

46. Tsuno, K. & Dasgupta, R. Melting phase relation of nominally anhydrous, carbonated pelitic-eclogite at 2.5–3.0 GPa and deep cycling of sedimentary carbon. *Contrib. Mineral. Petrol.* **161**, 743–763 (2011).
47. Villegas, E. A. *The Diffusion of Nitrogen in Liquid Iron Alloys at 1600°C.* PhD Thesis, Stanford Univ. (1976).
48. Dasgupta, R., Chi, H., Shimizu, N., Buono, A. S. & Walker, D. Carbon solution and partitioning between metallic and silicate melts in a shallow magma ocean: implications for the origin and distribution of terrestrial carbon. *Geochim. Cosmochim. Acta* **102**, 191–212 (2013).
49. Tsuno, K., Grewal, D. S. & Dasgupta, R. Core–mantle fractionation of carbon in Earth and Mars: the effects of sulfur. *Geochim. Cosmochim. Acta* **238**, 477–495 (2018).
50. Speelmanns, I. M., Schmidt, M. W. & Liebske, C. Nitrogen solubility in core materials. *Geophys. Res. Lett.* **45**, 7434–7443 (2018).
51. Walker, D., Dasgupta, R., Li, J. & Buono, A. Nonstoichiometry and growth of some Fe carbides. *Contrib. Mineral. Petrol.* **166**, 935–957 (2013).
52. Mosenfelder, J. L. et al. Nitrogen incorporation in silicates and metals: results from SIMS, EPMA, FTIR, and laser-extraction mass spectrometry. *Am. Mineral.* **104**, 31–46 (2019).
53. Li, Y., Dasgupta, R., Tsuno, K., Monteleone, B. & Shimizu, N. Carbon and sulfur budget of the silicate Earth explained by accretion of differentiated planetary embryos. *Nat. Geosci.* **9**, 781–785 (2016).
54. Kadik, A. A. et al. Solution behavior of reduced N–H–O volatiles in $FeO–Na_2O–SiO_2–Al_2O_3$ melt equilibrated with molten Fe alloy at high pressure and temperature. *Phys. Earth Planet. Inter.* **214**, 14–24 (2013).
55. Holzheid, A., Palme, H. & Chakraborty, S. The activities of NiO, CoO and FeO in silicate melts. *Chem. Geol.* **139**, 21–38 (1997).
56. Ma, Z. Thermodynamic description for concentrated metallic solutions using interaction parameters. *Metall. Mater. Trans. B* **32**, 87–103 (2001).
57. Rubie, D. C. et al. Heterogeneous accretion, composition and core–mantle differentiation of the Earth. *Earth Planet. Sci. Lett.* **301**, 31–42 (2011).
58. Deguen, R., Olson, P. & Cardin, P. Experiments on turbulent metal–silicate mixing in a magma ocean. *Earth Planet. Sci. Lett.* **310**, 303–313 (2011).
59. Deguen, R., Landeau, M. & Olson, P. Turbulent metal–silicate mixing, fragmentation, and equilibration in magma oceans. *Earth Planet. Sci. Lett.* **391**, 274–287 (2014).
60. McDonough, W. F. & Sun, S.-s The composition of the Earth. *Chem. Geol.* **120**, 223–253 (1995).
61. Yoshizaki, T. & McDonough, W. F. The composition of Mars. *Geochim. Cosmochim. Acta* **273**, 137–162 (2020).
62. Nittler, L. R., Chabot, N. L., Grove, T. L. & Peplowski, P. N. in *Mercury The View after* MESSENGER (eds Solomon S. C., Nittler L. R. & Andersen, B. J.) pp 30–51 (Cambridge Univ. Press, 2019).

Acknowledgements

The manuscript benefitted from constructive criticism from S. Mikhail. G. Costin is acknowledged for help with electron microprobe analyses. D.S.G. received support from NASA FINESST grant 80NSSC19K1538. NASA grants 80NSSC18K0828 and 80NSSC18K1314 to R.D. supported the work. D.S.G. acknowledges additional support from a Lodieska Stockbridge Vaughn Fellowship by Rice University.

Author contributions

D.S.G. conceived and developed the central ideas presented in this study. R.D. helped in refining the ideas. D.S.G. and R.D. designed the experiments. T.H. and D.S.G. performed the experiments. A.F. performed the FTIR analyses. D.S.G. analysed the experiments and developed the models. D.S.G. and R.D. interpreted the data. D.S.G. wrote the manuscript with inputs from R.D.

Competing interests

The authors declare no competing financial interests.

Additional information

Extended data is available for this paper at https://doi.org/10.1038/s41561-021-00733-0.

Supplementary information The online version contains supplementary material available at https://doi.org/10.1038/s41561-021-00733-0.

Correspondence and requests for materials should be addressed to D.S.G.

Peer review information *Nature Geoscience* thanks Sami Mikhail and the other, anonymous, reviewer(s) for their contribution to the peer review of this work. Primary Handling Editor: Rebecca Neely.

Reprints and permissions information is available at www.nature.com/reprints.

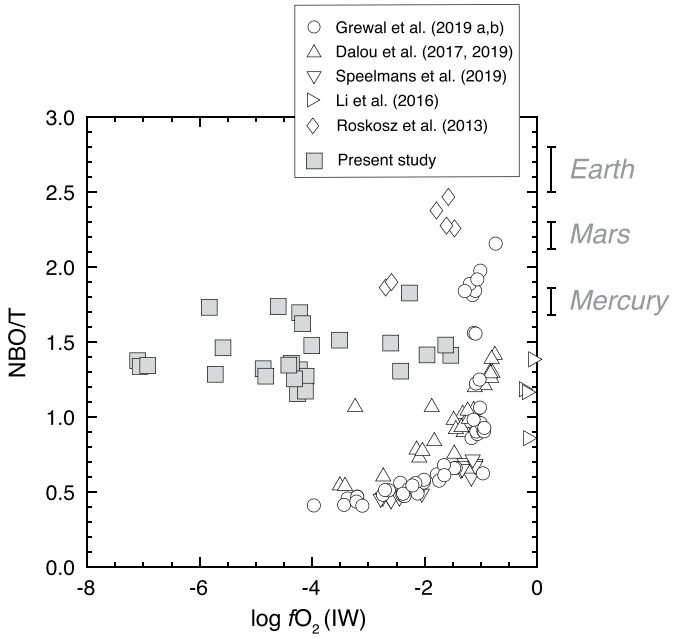

Extended Data Fig. 1 | Comparison of the silicate melt compositions of this study with previous studies as a function of oxygen fugacity. Below IW–1.5 (fO_2 range explored in this study), the silicate melt compositions of this study are more mafic, that is, have higher NBO/Ts, relative to the silicate melt compositions used to determine $D_N^{alloy/silicate}$ in previous studies. Therefore, the silicate melt compositions of this study are more representative of magma oceans of inner Solar System rocky planets. Primitive mantle compositions are used to estimate the magma ocean compositions of Earth[60], Mars[61] and Mercury[62]. NBO/T is a measure of degree of silicate melt polymerization and is expressed as total non-bridging oxygens per tetrahedral cations; NBO/T = (2 × Total O)/T – 4, where T = Si + Ti + Al + Cr + P). The calculated error bars for NBO/T represent ±1-σ deviation based on the replicate electron microprobe analyses and are smaller than the symbol sizes for all data from this study.

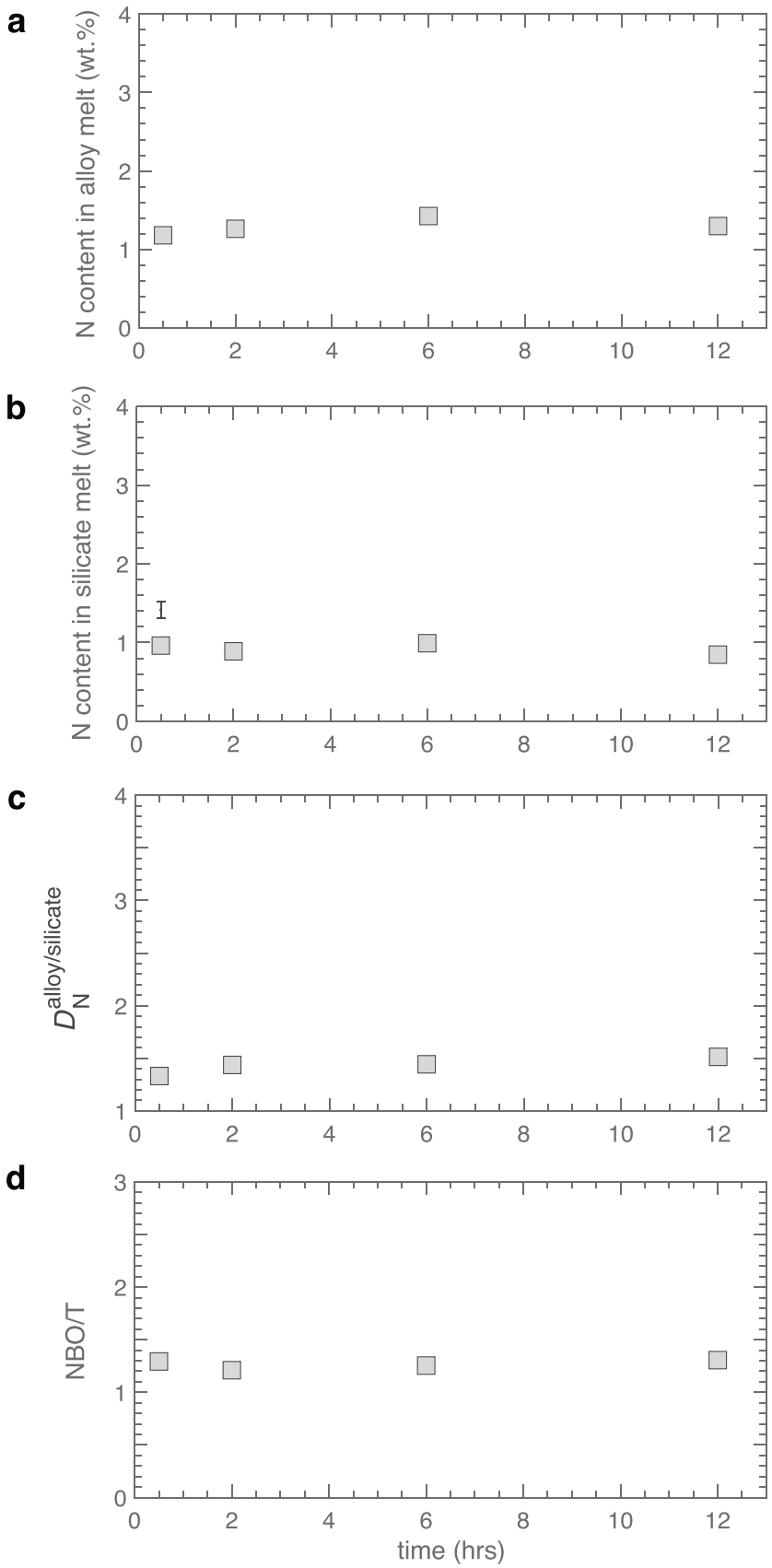

Extended Data Fig. 2 | See next page for caption.

Extended Data Fig. 2 | Time series to determine the experimental duration necessary to reach equilibrium. N contents in the (**a**) alloy and (**b**) silicate melts, and consequently (**c**) $D_N^{alloy/silicate}$ show no variation beyond the uncertainties of the measurements as a function of time for experiments conducted at 3 GPa and 1600 °C for 0.5, 2, 6, and 12 hours (Experiment numbers: X63, G634, X74, and G639). These demonstrate that N exchange between the two phases had attained equilibrium at less than 0.5 hours in our experimental conditions. Also, an almost unchanged N content in alloy and silicate melts with increase in time means that there was no loss of N from the alloy + silicate melt system with increase in experimental run time. **d,** NBO/T of the silicate melt compositions also show no variation with time beyond the uncertainties of the measurements, which illustrates that the silicate melt compositions had also reached steady state. All experiments were conducted with a fixed starting composition of alloy + silicate mixture (70%ThB1+30%Fe-5Ni-5N-17.5Si). Error bars in all panels are ±1-σ deviation based on replicate electron microprobe analyses and where absent the error bars are smaller than the symbol size.

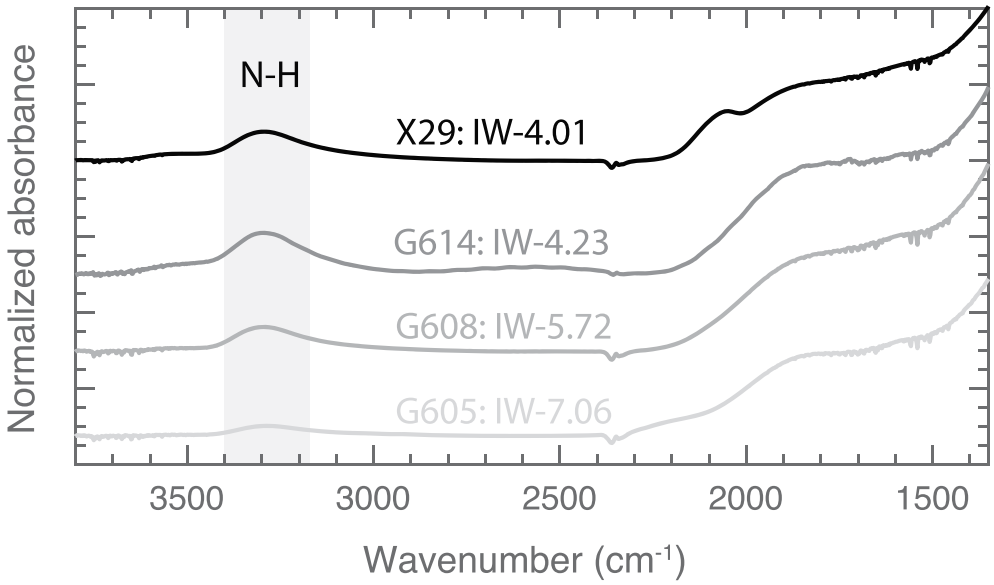

Extended Data Fig. 3 | Thickness normalized FTIR spectra of the peaks associated with nitrogen species in the experimental silicate glasses of this study. The only detectable, IR-active N-bearing peak was that of N-H stretching, marked by the grey band. No C-species were detectable.

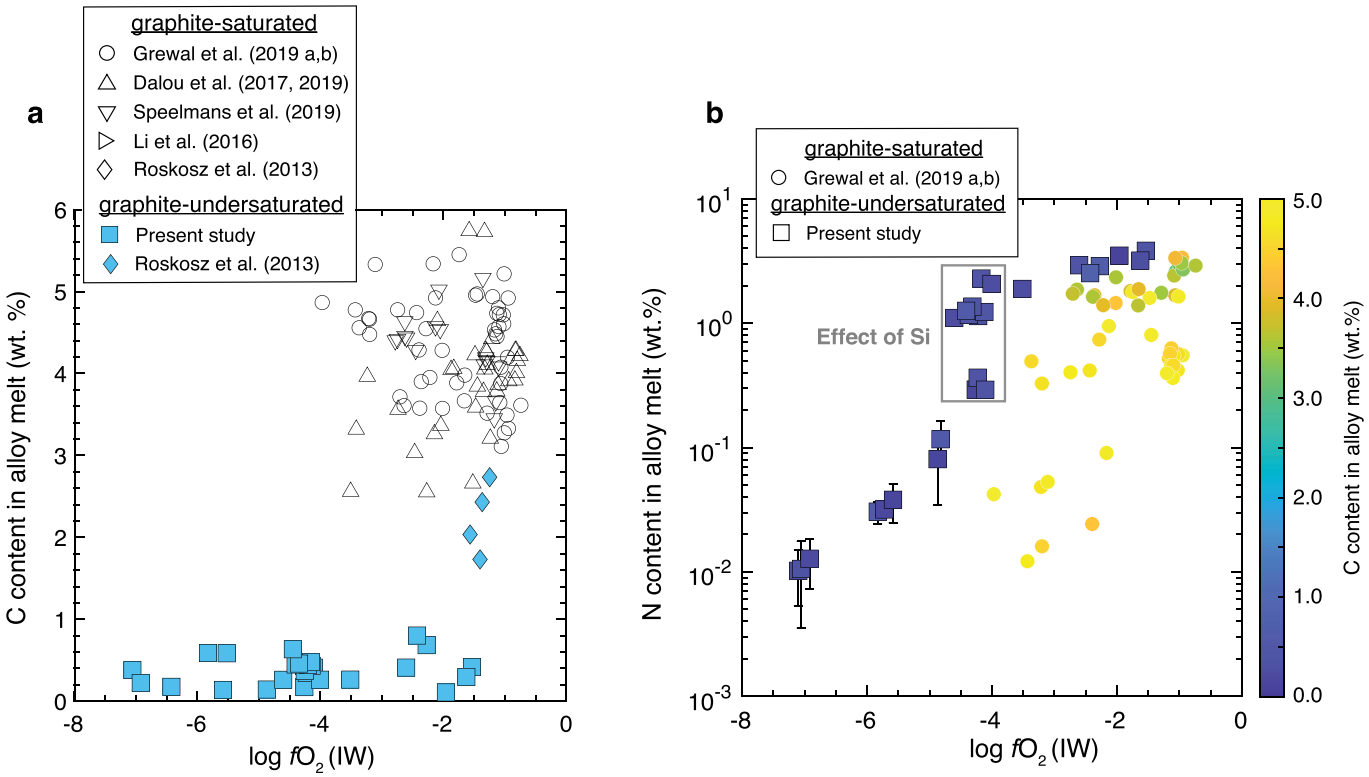

Extended Data Fig. 4 | Carbon and nitrogen contents in the alloy melts as a function of oxygen fugacity. a, C content in the alloy melt in graphite-undersaturated experiments of this study is substantially lower (0.11–0.80 wt.%) than the graphite-saturated experiments of the previous studies[10–13,22,27]. **b,** In agreement with previous studies in graphite-saturated conditions, N content in the alloy melt decreases with decrease in fO_2 in graphite-undersaturated conditions. However, at any given fO_2, N in graphite-undersaturated alloys is substantially greater than graphite-saturated alloys. $D_N^{alloy/silicate}$ for graphite-saturated alloys has been determined only in N-undersaturated conditions, therefore, N content in the alloys from only two previous studies[10,11] was compared with the data from the present study because of similar N contents in the starting mixtures. Error bars represent ±1-σ deviation based on the replicate electron microprobe analyses; where absent, the error bars are smaller than the symbol size.

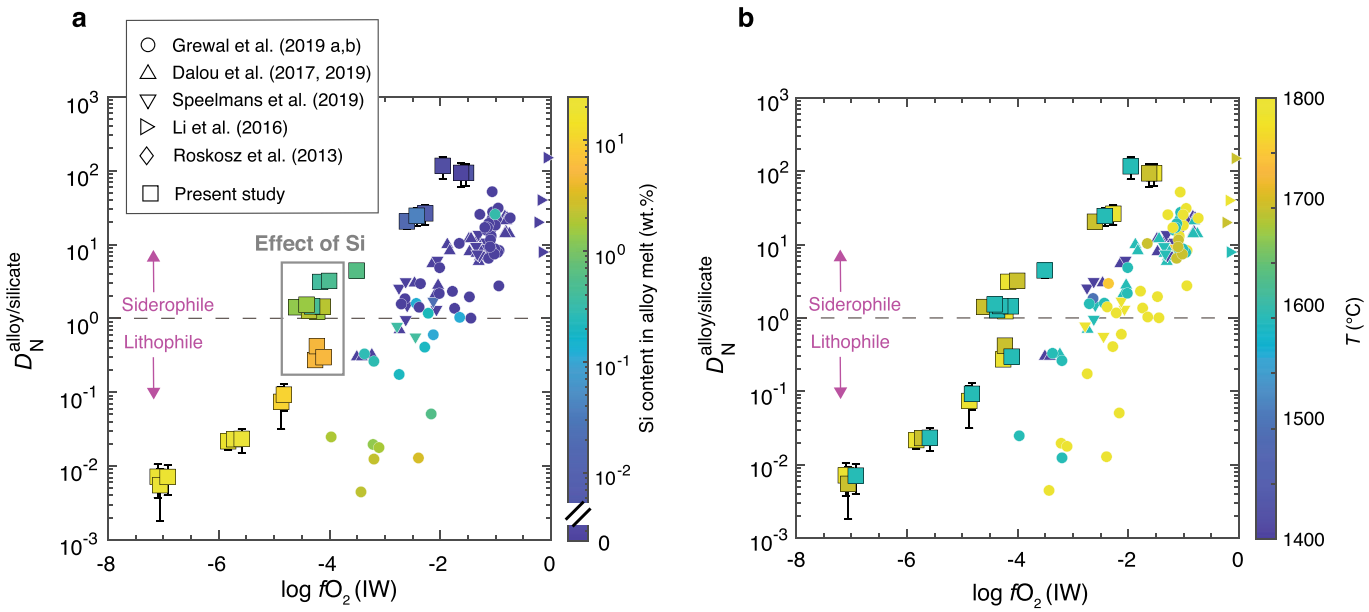

Extended Data Fig. 5 | $D_N^{alloy/silicate}$ as a function of oxygen fugacity and (a) silicon content in the alloy and (b) temperature. a, In addition to the effect of fO_2, when Si content in the alloy melt and FeO content in the silicate melt are coupled to each other, incorporation of Si into the alloy melt on its own has a strong negative effect on N content in the alloy at a similar logfO_2 (~IW−4; here shown by grey rectangle). A similar effect has been observed in a previous study[11] albeit at a higher logfO_2 (~IW−2.5) because in graphite-saturated alloys, Si expels N from the alloy melt even at low concentrations (as low as 0.1 wt.% Si). **b,** In contrast to the observations of previous studies[11,12] in graphite-saturated conditions, temperature does not have any discernible effect on $D_N^{alloy/silicate}$ in the limited temperature range explored in this study. Error bars represent ±1-σ deviation obtained by propagation of ±1-σ deviation on N content in the alloy and silicate melts; where absent, the error bars are smaller than the symbol size.

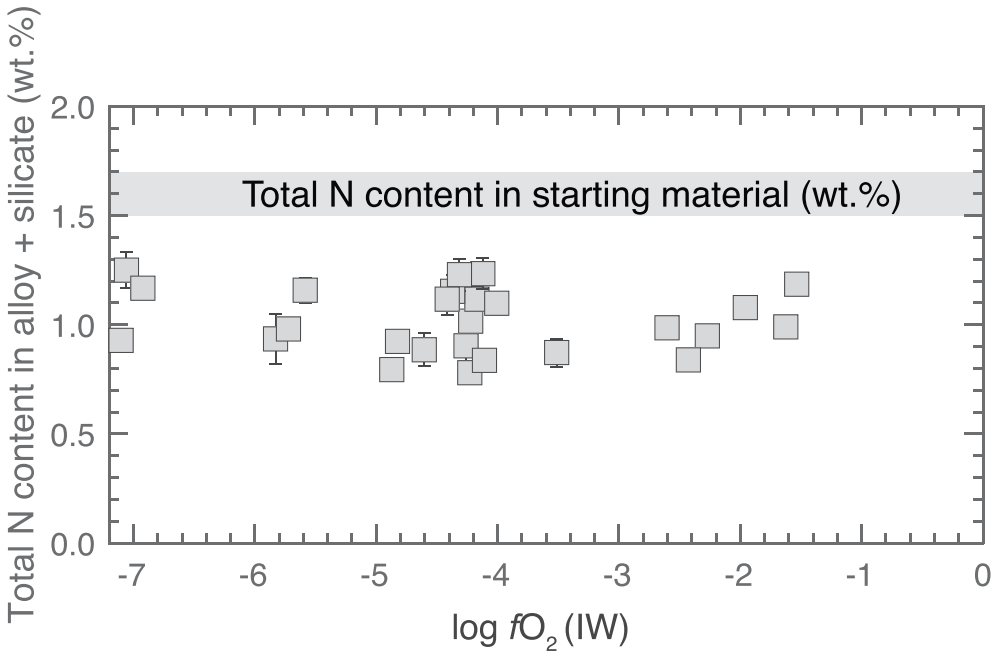

Extended Data Fig. 6 | Comparison between nitrogen content in the final products and starting mixtures. Similar to the observation in all previous studies that estimated $D_N^{alloy/silicate}$ in graphite capsules[10–13,22,27], the reconstructed N content in the final products of this study in MgO capsules is less than the N content in the starting mixture. Mass balance suggests that the extent of recovery of initial N content lies in the range of ~50–85%. Loss of N has been explained by the storage of N in the pores of the capsule walls or diffusive loss across the capsule wall[11,12]. Error bars represent ±1-σ deviation obtained by propagation of ±1-σ deviation on N content in the alloy and silicate melts; where absent, the error bars are smaller than the symbol size.

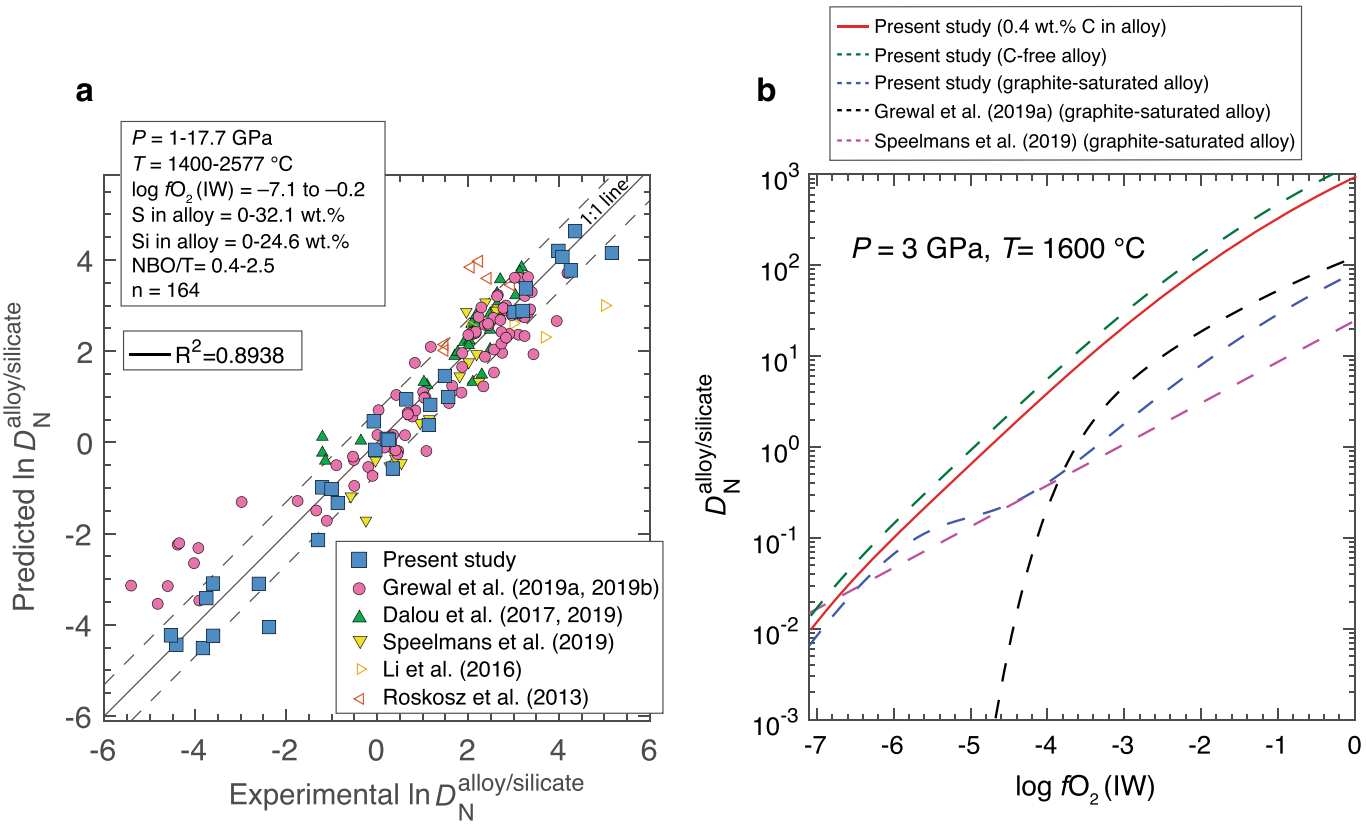

Extended Data Fig. 7 | Predicted $D_N^{alloy/silicate}$ using the parametrization developed in this study and comparison between the $D_N^{alloy/silicate}$ values predicted by this study and two previous studies. a, Predicted $D_N^{alloy/silicate}$ using the parametrization developed in this study plotted against experimentally determined $D_N^{alloy/silicate}$ for Fe-Ni-N±C±S±Si alloy melt-silicate melt equilibration. 'n' represents the total number of experiments that were used to calibrate the parameterized equation in this study. Solid line represents 1:1 fit while the dashed lines represent error within a factor of 2. **b,** The predicted $D_N^{alloy/silicate}$ values in C-free and graphite-undersaturated alloys, in agreement with the experimental data of this study, are an order of magnitude higher than the predicted $D_N^{alloy/silicate}$ values of graphite-saturated alloys at logfO_2> IW–5 and the gap between the predicted values decreases with decrease in fO_2 (see Methods).

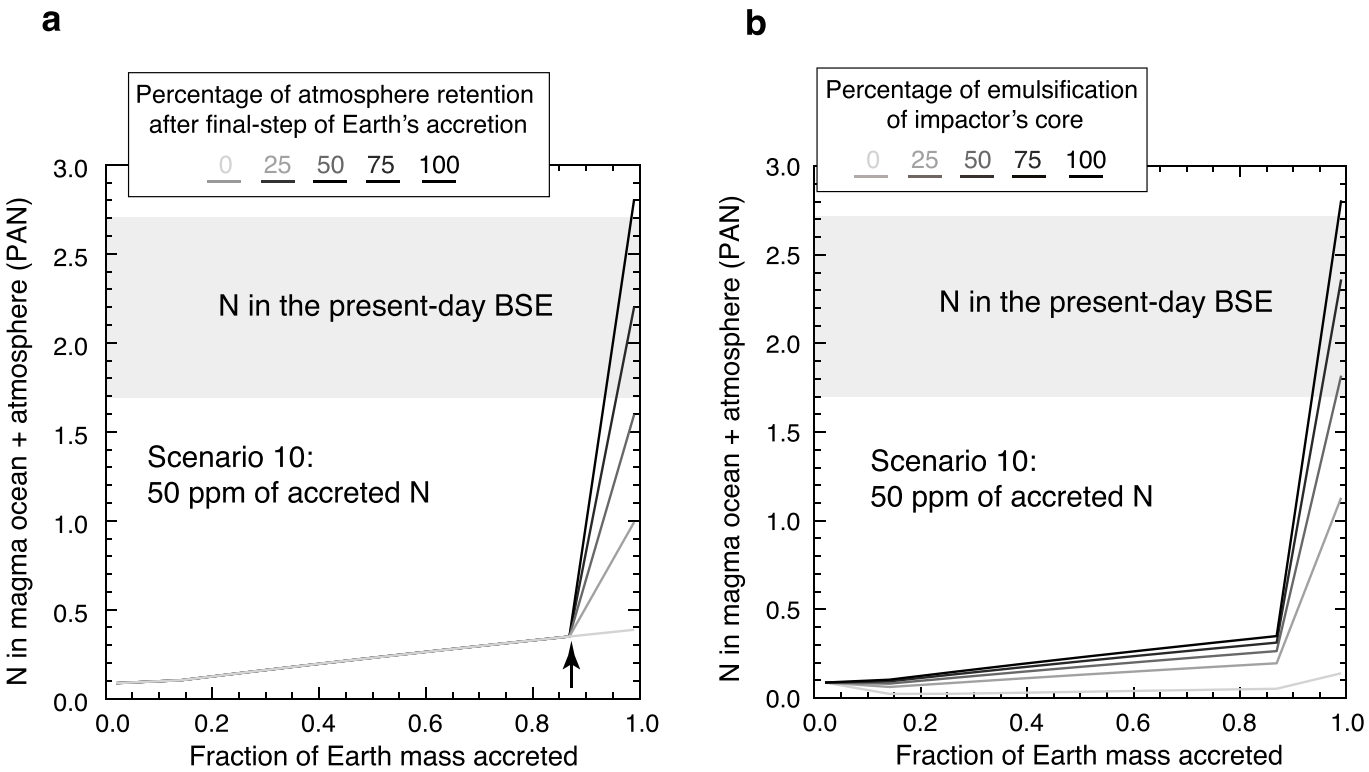

Extended Data Fig. 8 | The effects of (a) the extent of atmosphere retention after final-step of Earth's accretion and (b) the extent of emulsification of the impactor's core in the target's magma ocean on N budget of the BSE. For scenario 10 (as defined in Fig. 5a) and 50 ppm of accreted N, it can be seen that N budget of the present-day BSE can be satisfied for ~60–100 % of atmosphere retention on Earth after its final accretion event (**a**) and for ~50–100 % emulsification of the impactor's core in the target's MO (**b**) during every step of accretion. Lesser extent of final-stage atmospheric retention or lesser degree of emulsification of the impactor's core would require higher amount of accreted N (>50 ppm) in the seed planetary embryos (here Mars-sized) to satisfy the N budget of the present-day BSE.

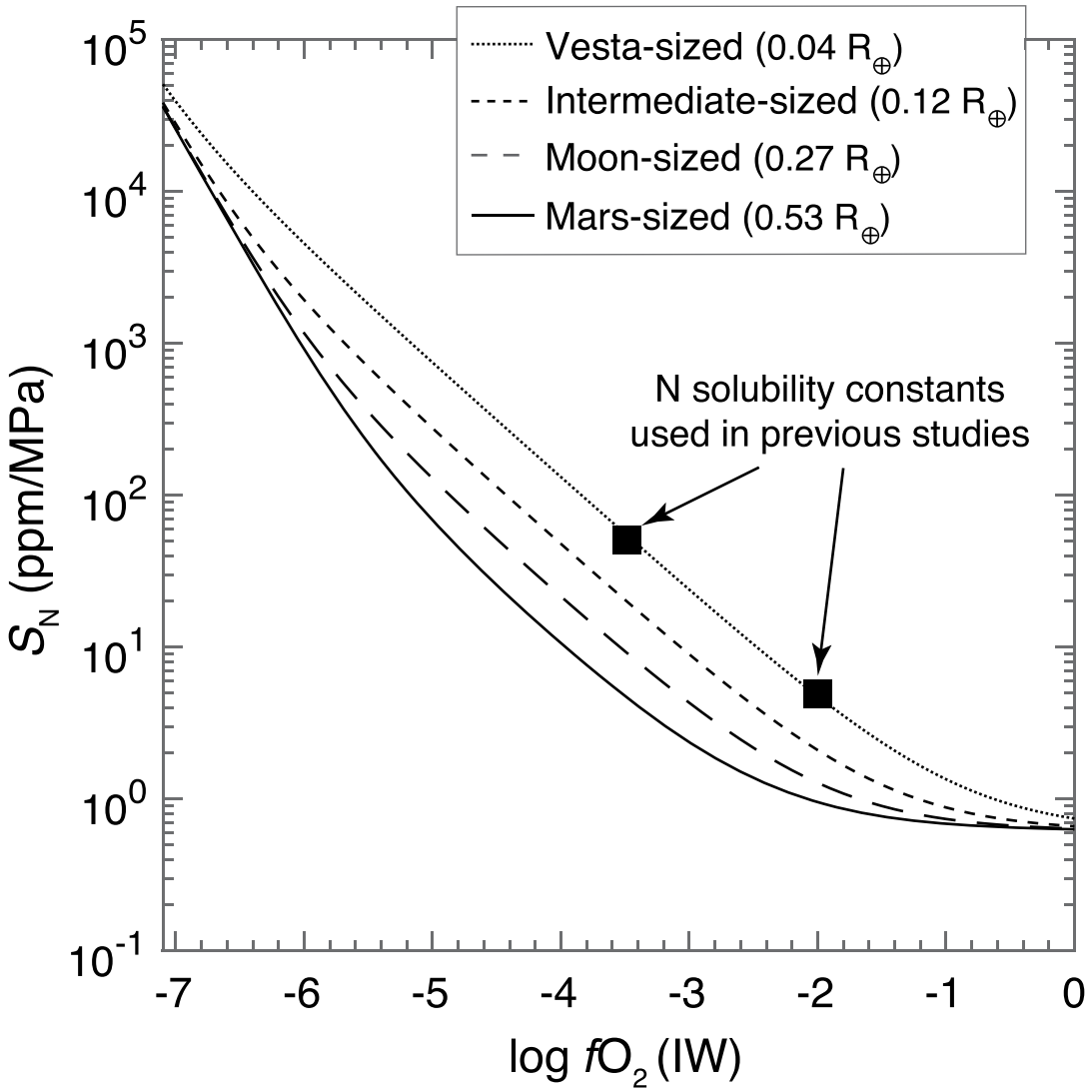

Extended Data Fig. 9 | Comparison between the calculated nitrogen solubility constants (S_N) from this study and the fixed values used in previous studies. The effective solubility constants for N vary with the size of protoplanetary bodies with variations in the range of an order of magnitude from a Vesta-sized to a Mars-sized protoplanet. Therefore, using a fixed solubility constant, as used in previous studies[3,4,10] to calculate the solubilities of N in magma oceans for rocky bodies having different sizes can give erroneous results.